



# Attenuating heave-induced pressure oscillations in offshore drilling by downhole flow control<sup>☆</sup>

Timm Strecker<sup>\*</sup>, Ole Morten Aamo

Department of Engineering Cybernetics, Norwegian University of Science and Technology (NTNU), Trondheim N-7491, Norway

## ARTICLE INFO

### Article history:

Received 30 November 2018  
 Received in revised form 5 April 2019  
 Accepted 1 May 2019  
 Available online 15 May 2019

### Keywords:

Disturbance rejection  
 Distributed-parameter systems  
 Flow control  
 Well control  
 Managed pressure drilling

## ABSTRACT

One of the challenges when applying managed pressure drilling (MPD) offshore on a floating rig is the wave-induced heaving motion of the rig. During drillstring extensions, the drillstring is rigidly attached to the rig and follows the rig's heaving motion. This induces pressure oscillations in the well that can violate pressure margins, in particular in rough conditions and when margins are tight. In order to enable drilling operations under such conditions, the pressure oscillations are to be attenuated by use of a controllable valve installed in the bottomhole assembly (BHA) at the bottom of the drillstring. The subject of this paper is the controller design for the valve flow based on measurements of the BHA movement and downhole pressure. Using a frequency-domain approach, the control law is designed to, in case of downwards BHA movement, reduce the valve flow to compensate the mud being displaced by the BHA and the flow due to mud clinging to the moving drillstring. Controlling the valve flow in such a manner creates large differential pressures over the valve that can potentially destabilize the BHA motion, which must be taken into consideration in the control design. Stability and performance of the closed-loop system are verified in simulations using a high-fidelity model of the drilling mud and elastic drillstring.

© 2019 Published by Elsevier Ltd.

## 1. Introduction

### 1.1. Managed pressure drilling

When drilling a well, fluid, often called drilling mud, is pumped down through the drillstring, through the bit and up the annulus. One of many purposes of the mud is to control the pressure in the well. It is essential to keep the pressure between the pore pressure and the fracture pressure of the formation to avoid detrimental events such as kick (undesired inflow of hydrocarbons into the well) or formation fracture. While upper parts of the well are protected by casing, the open-hole section in the lower part of the well is exposed to the formation. In challenging situations with tight margins between pore and fracture pressure, managed pressure drilling is often applied to enable faster and more flexible pressure control than is possible in conventional drilling, see e.g. (Hannegan, 2006; Rehm, Schubert, Haghshenas, Paknejad, & Hughes, 2013). In managed pressure drilling, a choke at the topside outflow of the annulus controls the mud pressure to a desired setpoint, which gives additional control over the pressure in the well besides the mud weight and frictional pressure drop.

In many situations, it is desired to control the pressure at the well bottom to within  $\pm 2.5$  bar of a setpoint (Godhavn, 2010). Automation and feedback control can enable such tight pressure control (Godhavn, 2010; Godhavn, Pavlov, Kaasa, & Rolland, 2011; Stamnes, Zhou, Kaasa, & Aamo, 2008). One of the challenges in pressure control are disturbances, such as drill string movements. Drillstring movements when running into or pulling out of the hole have long been known to induce pressure oscillations that can potentially violate pressure margins (Burkhardt, 1961; Mitchell, 1988; Samuel, Sunthankar, McColpin, Bern, Flynn, et al., 2003; Wagner, Halal, Goodman, et al., 1993).

### 1.2. Heave-induced pressure oscillations

When drilling offshore from a floating rig, a different form of drillstring movement occurs due to the wave-induced heaving motion of the rig. When extending the drillstring by a segment, the heave compensators that usually decouple the string mechanically from the rig's heave motion are disabled, and the drillstring oscillates with the waves. The modeling and prediction of heave-induced pressure oscillations have been the subject of research over the last years (Aarsnes, Gleditsch, Aamo, & Pavlov, 2014; Landet, Pavlov, & Aamo, 2013; Strecker, Aamo, & Manum, 2017). Since the period of the heave motion is roughly in the same range as the time it takes pressure waves to propagate through the well, it has been identified that distributed-parameter models are

<sup>☆</sup> This work was supported by Equinor, Norway.

<sup>\*</sup> Corresponding author.

E-mail addresses: [tim.strecker@unimelb.edu.au](mailto:tim.strecker@unimelb.edu.au) (T. Strecker), [aamo@ntnu.no](mailto:aamo@ntnu.no) (O.M. Aamo).

required to accurately capture the dynamics, and attempts using low-order lumped models, which have successfully attenuated the effect of slow drillstring movements, have failed (Pavlov, Kaasa, & Imsland, 2010).

Efforts on attenuating heave-induced pressure oscillations have so far focused on controlling the opening of the topside choke (Aamo, 2013; Albert, Aamo, Godhavn, & Pavlov, 2015; Landet et al., 2013; Mahdianfar, Hovakimyan, Pavlov, & Aamo, 2016; Strecker & Aamo, 2017b, 2017c). Since circulation usually needs to be stopped when extending the drillstring, the opening of the topside choke is basically the only control input available without additional instrumentation. While control from topside can achieve an improvement in some situations, the fact that the control signal has to overcome a significant amount of friction as it propagates kilometers through the well, and the delay before it reaches the well bottom, impose limitations on the achievable performance of this approach (Strecker & Aamo, 2017a, 2018). Moreover, even if an improvement is achieved at the well bottom, disturbance rejection from topside creates a pressure amplitude profile along the well that can make things worse at other locations in the well (Aarsnes, Aamo, Hauge, & Pavlov, 2013; Strecker & Aamo, 2018).

### 1.3. Contribution and outline

This paper presents a new approach to attenuating heave-induced pressure oscillations. Here, circulation is maintained during drillstring connections, and an instrument comprising a controllable valve as well as acceleration and pressure sensors and a computing unit is installed in the bottomhole assembly. Flow disturbances induced by the heave motion are compensated by controlling the flow through the controllable valve. We present the design of a control law that computes the desired valve flow based on the measured movement. Installing both sensor and actuator downhole has two main advantages over control from topside. First, the actuator is at or very close to where pressure control is desired. Thus, there is practically no delay and no friction that affects the control input before it reaches the control objective. Second, the motion of the drillstring bottom, which is the main cause of the downhole pressure oscillations, is measured directly. Therefore, the system does not rely on being able to accurately predict the movement of the elastic drillstring. Since no information exchange between the controllable valve and the rig is required – other than perhaps start/stop signals – it can work autonomously.

One of the challenges when controlling the valve flow in such a manner is that it creates large differential pressures, resulting in a force on the BHA that is in phase with the BHA movement. In order to avoid amplifying, or even destabilizing the drillstring motion, the control law must be designed to avoid exciting resonant frequencies of the elastic drillstring and the mud column inside the string.

In a few situations, it can happen that pressure oscillations remain in the annulus that are only slowly dampened by friction. For such cases, we present a pressure feedback scheme to improve attenuation of the oscillations.

The paper is organized as follows. In Section 2, we present a high fidelity model consisting of a set of coupled hyperbolic differential equations for the dynamics of the drilling mud both inside the drillstring and in the annulus, as well as the elastic drillstring. Section 3 contains the design of low-order controllers for attenuating the pressure oscillations based on BHA motion measurements. In particular, four different designs are presented and their stability and performance properties are compared. Performance and stability for the two most recommendable designs are further analyzed in Section 4, including the sensitivity

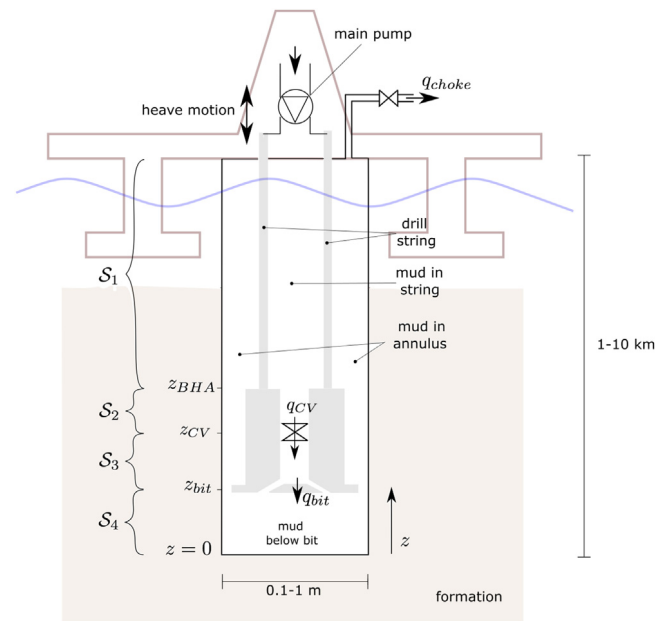


Fig. 1. Well schematic.

Table 1  
List of variables and subscripts.

Symbol		Subscript	
$p$	Pressure	$a$	Mud in annulus
$q$	Flow rate	$i$	Mud inside drillstring
$A$	Cross sectional area	$d$	Drillstring or BHA
$\beta$	Bulk modulus	$b$	Mud below bit
$F$	Friction force per meter	$rig$	Rig
$\sigma$	Drillstring stress	$mp$	Main pump
$v$	Velocity	$CV$	Controllable valve
$\epsilon$	Drillstring strain	$acc$	Accumulator

with respect to uncertainty, the parameterization of controller parameters over well length when drilling a long well section, and the system behavior in non-vertical wells. In Section 5, we construct a case in which the remaining pressure oscillations with BHA-movement-to-flow control are still significant, and design a pressure feedback control to improve attenuation of the pressure oscillations. Finally, concluding remarks are given in Section 6, and several system coefficients are given in the appendix.

## 2. Modeling

A schematic of a well of length  $L$  is depicted in Fig. 1. We divide the well into 4 different sections: Section  $S_1$  comprises the section between topside and the top of the bottomhole assembly (BHA), section  $S_2$  reaches from the top of the BHA to the position where the controllable valve is installed, section  $S_3$  is from the controllable valve to the drillbit (at the BHA bottom) and section  $S_4$  is the section below the bit. If required, the model can easily be extended by more sections to include, for instance, heavy weight drill pipe between the BHA and drill string.

The axial position,  $z$ , is measured from the bottom of the well and is kept stationary relative to earth. Although the position of the drill string and BHA oscillates with the heave motion, this movement is very small compared to the well length (less than  $\pm 5$  m compared to several km). Therefore,  $z_{bit}$ ,  $z_{CV}$  and  $z_{BHA}$  are considered time invariant for simplicity.

Following the approach in Mitchell (1988) and Strecker et al. (2017), the mud and drillstring dynamics in each section are

modeled as coupled hydraulic transmission lines. Mathematically, these are described by a set of coupled wave-type hyperbolic partial differential equations (PDEs), with coupling terms at the section boundaries. This type of PDE model has been verified by field data from surge-swab operations in Samuel et al. (2003) and Wagner et al. (1993). More recently, (Kvernland, Gorski, Sant'Ana, Godhavn, Aamo, Sangesland, et al., 2019) reported a very good match between the model from (Strecker et al., 2017) and pressure data from a well with heave (see also Figs. 5–7 and Table 1 in Kvernland et al. (2019)). A good overview over hydraulic transmission line models is also given in Stecki and Davis (1986a, 1986b).

## 2.1. Distributed dynamics

The dynamics in each well section  $S_j$ ,  $j = 1, 2, 3$ , are governed by the following set of 6 coupled partial differential equations which model distributed mass and momentum balances for the elastic drillstring (or BHA, respectively), mud in annulus and mud inside the string:

$$\frac{\partial p_{a,j}}{\partial t} = -\frac{\beta_{a,j}}{A_{a,j}} \frac{\partial q_{a,j}}{\partial z} - \frac{\beta_{a,j}}{A_{a,j}} \frac{\partial A_{a,j}}{\partial p_{i,j}} \frac{\partial p_{i,j}}{\partial t} \quad (1)$$

$$\frac{\partial q_{a,j}}{\partial t} = -\frac{A_{a,j}}{\rho} \frac{\partial p_{a,j}}{\partial z} - \frac{1}{\rho} F_{a,j}(q_{a,j}, v_{d,j}) - A_{a,j}g \quad (2)$$

$$\frac{\partial p_{i,j}}{\partial t} = \frac{\beta_{i,j}}{A_{i,j}} \frac{\partial q_{i,j}}{\partial z} - \frac{\beta_{i,j}}{A_{i,j}} \frac{\partial A_{i,j}}{\partial p_{a,j}} \frac{\partial p_{a,j}}{\partial t} \quad (3)$$

$$\frac{\partial q_{i,j}}{\partial t} = \frac{A_{i,j}}{\rho} \frac{\partial p_{i,j}}{\partial z} - \frac{1}{\rho} F_{i,j}(q_{i,j}, v_{d,j}) - A_{i,j}g \quad (4)$$

$$\frac{\partial \sigma_{d,j}}{\partial t} = E \left( \frac{\partial v_{d,j}}{\partial z} + \frac{\partial \epsilon_{z,j}}{\partial p_{i,j}} \frac{\partial p_{i,j}}{\partial t} + \frac{\partial \epsilon_{z,j}}{\partial p_{a,j}} \frac{\partial p_{a,j}}{\partial t} \right) \quad (5)$$

$$\frac{\partial v_{d,j}}{\partial t} = \frac{1}{\rho} \frac{\partial \sigma_{d,j}}{\partial z} - \frac{1}{\rho A_{d,j}} (F_{mech,j}(v_{d,j}) + F_{d,j}(q_{a,j}, q_{i,j}, v_{d,j})) - A_{d,j}g \quad (6)$$

Here, the subscripts indicates the subsystem ( $a$  for mud in annulus,  $i$  for mud inside string,  $d$  for elastic drillstring ( $j = 1$ ) and BHA ( $j = 2, 3$ )),  $p$  is mud pressure,  $q$  is volumetric flow rate (relative to earth),  $\sigma_d$  is the drillstring stress,  $\epsilon_z$  the drillstring strain in axial direction,  $v_d$  the drillstring velocity (relative to earth),  $\beta$  is the effective bulk modulus,  $A$  is cross sectional area,  $\rho$  is density,  $F$  are friction forces and  $g$  is gravitational acceleration. See also Table 1 for nomenclature. For brevity, we omitted the argument  $(z, t)$  behind the system states in (1)–(6), and assume that all parameters are constant along each section, although all steps in this paper can easily be generalized to consider space-varying parameters. Formulas for the coefficients modeling pressure-induced pipe ballooning and length changes are given in Appendix A. The model for the section below the bit  $S_4$  is similar but simpler, as it is purely fluid-filled without any drillstring or BHA. Mass and momentum for the mud balances are

$$\frac{\partial p_b}{\partial t} = -\frac{\beta_b}{A_w} \frac{\partial q_b}{\partial z} \quad (7)$$

$$\frac{\partial q_b}{\partial t} = -\frac{A_b}{\rho} \frac{\partial p_b}{\partial z} - \frac{1}{\rho} F_b(q_b) - Ag. \quad (8)$$

**Remark 1.** While the distributed dynamics are very pronounced in all states in section  $S_1$ , the BHA, in contrast, behaves almost like a rigid body for the parameters used in this paper. However, in order to be able to directly apply the method to other cases, for instance when  $S_2$  represents a several hundred meter long heavy-weight drill pipe section, or when the bit is far from the well bottom, we use the transmission line PDE model for each well section.

**Remark 2.** Details of individual tools in the BHA are neglected in the model above, and the BHA is essentially modeled as a restriction of the flow area. Briefly speaking, if the frictional pressure drop over the BHA is large (say, 15 bar), then it can be impossible to control the pressure both above and below the BHA to within a specified window around a setpoint (say, within  $\pm 5$  bar) at the same time, even without heave. Therefore, such a case will be extremely challenging to drill with any technology. On the other hand, if the frictional pressure drop over the BHA is not very significant, it is fair to neglect some details of the BHA shape and approximate it as an approximately smooth flow restriction.

## 2.2. Boundary and coupling conditions

The PDE system (1)–(8) is completed by the following set of boundary and coupling conditions. Here, the rig vertical velocity  $v_{rig}$  is an external disturbance. The flow through the controllable valve,  $q_{CV}$ , is the control input. In this paper we assume that the valve opening can be controlled sufficiently fast to provide any desired flow, and treat  $q_{CV}$  as the control input rather than e.g. the valve opening or an opening/closing force.

The boundary conditions at the top of the well are governed by the heaving motion of the rig, the inflow from the main pump and the outflow through the annular choke. Here, the topside position of the annulus is kept static relative to earth whereas the drillstring top moves with the heaving rig. An accumulator partially filled with air is installed at the outlet of the main pump in order to smoothen potential pressure oscillations inside the drillstring. The air pressure inside the accumulator is governed by the ideal gas law, i.e.  $V_{air,acc} p_{air,acc} = c_{acc}$  is constant, and we have  $V_{acc} = V_{mud,acc} = V_{air,acc}$ . The topside mud pressure inside the string is assumed to be equal to the gas pressure. This gives for the topside boundary conditions

$$q_{a,1}(L, t) = q_{choke}(t) \quad (9)$$

$$\dot{V}_{mud,acc}(t) = q_{mp} - q_{i,1}(L, t) - A_{i,1}v_d(L, t) \quad (10)$$

$$p_{i,1}(L, t) = \frac{c_{acc}}{V_{acc} - V_{mud,acc}} \quad (11)$$

$$v_{d,1}(L, t) = v_{rig}(t) \quad (12)$$

where  $q_{mp}$  is the main pump flow rate (assumed to be constant) and the flow through the annular choke,  $q_{choke}$ , is modeled by a valve equation of the form

$$q_{choke}(t) = c_{choke} \sqrt{\frac{p_a^1(L, t) - 1[\text{bar}]}{\rho}}. \quad (13)$$

In practice, the choke flow is determined by a separate control system for the choke opening but, as this choke control loop is much slower than the heave disturbance, we treat choke coefficient  $c_{choke}$  as a constant in this paper.

According to Bernoulli's principle, there is a discontinuity in the mud pressure at locations where flow areas change. However, these discontinuities are magnitudes smaller than the pressure fluctuations caused by heave, and are neglected in the following. Thus, the coupling condition at the upper BHA end are governed by continuity of mud pressures and string velocity, force balance at the transition from drillstring to BHA, as well as the flow balance induced by the moving area change. For brevity, we introduce the notation  $p_{a,1}^{zBHA} = p_{a,1}(z_{BHA}, t)$  for all  $t$  and  $A_{a,1-2} = A_{a,1} - A_{a,2}$ . This gives

$$p_{a,1}^{zBHA} = p_{a,2}^{zBHA} \quad (14)$$

$$p_{i,1}^{zBHA} = p_{i,2}^{zBHA} \quad (15)$$

$$A_{d,1}\sigma_{d,1}^{zBHA} = \sigma_{d,2}^{zBHA} A_{d,2} + p_{a,1}^{zBHA} A_{a,1-2}$$

**Table 2**  
Nominal parameters.

$L$	4000 m	$E$	200 GPa	$\tau_0$	10 Pa
$z_{bit}$	10 m	$E_f$	50 GPa	$K$	30 mPa·s
$z_{CV}$	60 m	$\rho$	1580 kg/m <sup>3</sup>	$n$	1
$z_{BHA}$	110 m	$\rho_d$	7800 kg/m <sup>3</sup>	$q_{mp}$	1.5 m <sup>3</sup> /min
$r_w$	0.1079 m	$c_{choke}$	10 <sup>-3</sup> m <sup>2</sup>	$\nu$	0.3
$\beta$	2 GPa	$c_{bit}$	7.5 × 10 <sup>-4</sup> m <sup>2</sup>	$\nu_f$	0.2

$$+ p_{i,1}^{z_{BHA}} A_{i,1-2} \quad (16)$$

$$q_{a,1}^{z_{BHA}} = q_{a,2}^{z_{BHA}} + A_{a,1-2} v_{d,2}^{z_{BHA}} \quad (17)$$

$$q_{i,1}^{z_{BHA}} = q_{i,2}^{z_{BHA}} - A_{i,1-2} v_{d,2}^{z_{BHA}} \quad (18)$$

$$v_{d,1}^{z_{BHA}} = v_{d,2}^{z_{BHA}} \quad (19)$$

The coupling condition at  $z_{CV}$  is similar to the one at  $z_{BHA}$ , but here we have  $q_{CV}$  as an input

$$p_{a,2}^{z_{CV}} = p_{a,3}^{z_{CV}} \quad (20)$$

$$p_{i,2}^{z_{CV}} A_{i,2} - \sigma_{d,2}^{z_{CV}} A_{d,2} = p_{i,3}^{z_{CV}} A_{i,3} - \sigma_{d,3}^{z_{CV}} A_{d,3} \quad (21)$$

$$q_{a,2}^{z_{CV}} = q_{a,3}^{z_{CV}} + A_{a,2-3} v_{d,3}^{z_{CV}} \quad (22)$$

$$q_{i,2}^{z_{CV}} = q_{CV} - A_{i,2} v_{d,2}^{z_{CV}} \quad (23)$$

$$q_{i,3}^{z_{CV}} = q_{CV} - A_{i,3} v_{d,3}^{z_{CV}} \quad (24)$$

$$v_{d,2}^{z_{CV}} = v_{d,3}^{z_{CV}} \quad (25)$$

At the drill bit (BHA bottom), mud flow rates are governed by the flow through the bit,  $q_{bit}$ , and the dashpot-like effect of the moving BHA, mud pressure below and around the BHA is assumed continuous, and the pressure forces on the BHA determine the mechanical stress at the BHA bottom

$$q_{i,3}^{z_{bit}} = q_{bit} - A_{i,3} v_{d,3}^{z_{bit}} \quad (26)$$

$$q_b^{z_{bit}} = -q_{bit} + q_{a,3}^{z_{bit}} + A_{d+i,3} v_{d,3}^{z_{bit}} \quad (27)$$

$$p_b^{z_{bit}} = p_{a,3}^{z_{bit}} \quad (28)$$

$$p_b^{z_{bit}} A_{d+i,3} = p_{i,3}^{z_{bit}} A_{i,3} - \sigma_{d,3}^{z_{bit}} A_{d,3} \quad (29)$$

The flow through the bit is modeled by a valve equation

$$q_{bit}(t) = c_{bit} \sqrt{\frac{p_{i,3}(z_{CV}, t) - p_b(z_{CV}, t)}{\rho}} \quad (30)$$

There is a no-flow boundary condition at the well bottom,

$$q_b(0, t) = 0. \quad (31)$$

### 2.3. Model parameters

Throughout this paper, unless stated otherwise, we use the well parameters given in Table 2 and as outlined in the following. We assume that the well has a constant diameter  $r_w$ , as given in Table 2, is vertical and that the drillstring is concentric in the well. Thus, the cross sectional areas are

$$A_{i,j} = \pi r_{di,j}^2 \quad A_{d,j} = \pi (r_{do,j}^2 - r_{di,j}^2) \quad (32)$$

$$A_{a,j} = \pi (r_w^2 - r_{do,j}^2) \quad A_b = \pi r_w^2, \quad (33)$$

for  $j = 1, 2, 3$ , where  $r_{di,j}$  and  $r_{do,j}$  are the inner and outer drillstring/BHA diameters, respectively, and are given in Table 3.

The friction terms are determined by the mud properties and the well geometry. The Herschel–Bulkley model (Herschel & Bulkley, 1926) is widely used to model the rheology of drilling fluids, and has become the recommended standard in the drilling

**Table 3**  
Well geometry.

	$S_1$	$S_2$	$S_3$
$r_{do,j}$	0.0635 m	0.0698 m	0.0698 m
$r_{di,j}$	0.0546 m	0.0381 m	0.0381 m

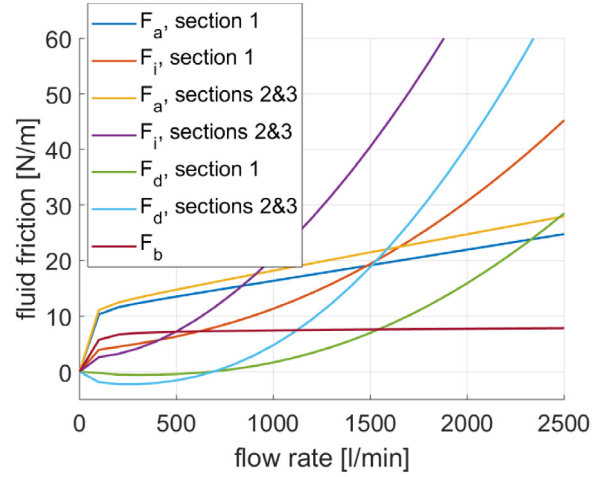


**Fig. 2.** Viscous friction forces on mud column and on drill string for constant flow rates and stationary drill string.

industry (API Recommended Practice 13D, 2006). It relates the shear rate  $\dot{\gamma}$  to the shear stress  $\tau$  by

$$\tau(\dot{\gamma}) = \begin{cases} \left( K |\dot{\gamma}|^{n-1} + \frac{\tau_0}{|\dot{\gamma}|} \right) \dot{\gamma} & \text{if } |\tau| > \tau_0 \\ \dot{\gamma} = 0 & \text{if } |\tau| \leq \tau_0 \end{cases} \quad (34)$$

where  $\tau_0$ ,  $K$  and  $n$  are the yield point, consistency index and flow index of the fluid, respectively. That is, the shear stress has to overcome the yield point before the fluid shears. The case  $n = 1$ , which we are using in this paper, is often called Bingham fluid, in which case  $K$  is called the plastic viscosity. Since flow in the annulus is laminar under the given flow rates and geometry, we apply the methodology developed in Strecker et al. (2017) to construct the friction terms  $F_{a,j}$  and  $F_b$ , which are shown in Fig. 2 for a stationary drill string. Briefly speaking, the friction terms are obtained using curve fitting and data obtained from 2D simulations of the fluid velocity profile over the annulus cross section. The effect of mud being accelerated by sticking to the moving string is taken into account by formulating friction as a function of the fluid velocity relative to the drillstring velocity. Therefore, friction forces also depend on the drill string velocity. See Strecker et al. (2017) for more details.

Inside the drillstring, the flow rate is large enough to induce turbulence. Therefore, the method from (Strecker et al., 2017) is not applicable since it assumes laminar flow. Instead, we use the friction terms from (API Recommended Practice 13D, 2006) for fluid friction inside the drillstring, which are also shown in Fig. 2.

In vertical wells, it is assumed that there is no contact force between the drillstring and the formation. Thus,  $F_{mech} = 0$  in vertical wells. In non-vertical wells, however, gravity and bending forces lead to a contact force between string and formation. In such cases, we apply the formula from (Aadnoy & Andersen, 1998). Briefly, mechanical drag is modeled as

$$F_{mech}(v_d) = \mu N \text{sign}(v_d) \quad (35)$$

where  $\mu$  is a friction factor and  $N$  is the normal force of the string acting on the formation.

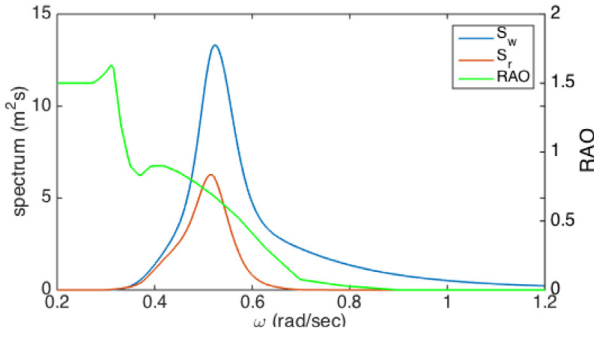


Fig. 3. Wave elevation spectrum  $S_w$  according to the Jonswap spectrum with significant wave height 6 m and peak period 12 s, response amplitude operator of a semisubmersible rig and rig response spectrum  $S_r$ .

#### 2.4. Heave motion

Waves are usually characterized via the spectrum of the wave elevation. For the North Sea, the Jonswap spectrum (Hasselmann, Barnett, et al., 1973) has been developed based on curve fitting and observational data. The Jonswap wave spectrum  $S_w$  for a significant wave height of 6 m and 12 s peak period is depicted in Fig. 3. The actual motion of the drilling rig also depends on the response amplitude operator (RAO) of the rig, which describes the rig motion response to waves depending on the frequency. Many semisubmersible drilling rigs that are used in rough conditions are designed to have a small RAO, in particular at high frequencies, such as the one depicted in Fig. 3. The rig response spectrum  $S_r$  is given by

$$S_r(\omega) = S_w(\omega)RAO^2(\omega). \quad (36)$$

Almost all of the energy in  $S_r$  in the example in Fig. 3 is in the frequency range  $0.35 \leq \omega \leq 0.65$  rad/second, corresponding to periods from approximately 9.5 to 18 s. It should be noted that other drilling platforms, such as drilling ships, can have a larger RAO in the frequency range of the waves, resulting in a larger response spectrum. Since the boundary condition (12) is expressed in terms of velocity rather than elevation, we require spectrum of the vertical rig velocity,  $S_v$ , which is given by

$$S_v(\omega) = \omega^2 S_r(\omega). \quad (37)$$

#### 2.5. Transfer functions

The controller design in this paper and part of the performance analysis will be completed in the frequency domain. For this purpose, the state-space model (1)–(8) is linearized around the steady state determined according to a fixed pump flow rate  $q_{mp}$  and  $v_{rig} = 0$ . That is, all flows inside the drillstring and in the annulus are equal to  $q_{mp}$ , the drillstring velocity and  $q_b$  are zero. The steady state pressures at each location are determined by integrating the hydrostatic and frictional pressure gradient against the flow direction starting from the annular choke. Then, the nonlinearities in the friction terms, in the valve equations for the bit and annular choke, and in the equation for the accumulator pressure are linearized around steady state. The pump flow rate is kept sufficiently high such that the flow disturbance due to heave never reverses the flow direction, keeping the flow rate away from the strong friction nonlinearities at zero flow in Fig. 2.

Next, we Laplace-transform the linearized system to obtain the transfer functions from the external input  $v_{rig}$  and the control input  $q_{CV}$  to the bottomhole pressure

$$p_0(t) = p_b(0, t), \quad (38)$$

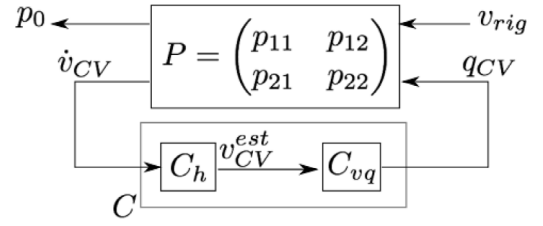


Fig. 4. Block diagram of the closed-loop system. The lower block indicates the controller  $C$  consisting of the heave integrator  $C_h$  and the velocity-estimate to flow controller  $C_{vq}$ .

which is to be kept at the setpoint by control, and to the measurement

$$\dot{v}_{CV} = \dot{v}_{d,2}^{zCV}. \quad (39)$$

Let  $P(s) = \begin{pmatrix} p_{11}(s) & p_{12}(s) \\ p_{21}(s) & p_{22}(s) \end{pmatrix}$  denote the open-loop transfer function, i.e. (see also Fig. 4)

$$\begin{pmatrix} p_0(s) \\ \dot{v}_{CV}(s) \end{pmatrix} = P(s) \begin{pmatrix} v_{rig}(s) \\ q_{CV}(s) \end{pmatrix}. \quad (40)$$

The closed-loop transfer function from  $v_{rig}$  to  $p_0$  is

$$G_{cl}(s) = p_{11}(s) + p_{12}(s)C(s)(1 - p_{22}(s)C(s))^{-1}p_{21}(s). \quad (41)$$

Using this, the root mean square of the bottomhole pressure, which is a reasonable performance measure, is given by

$$\text{rms}(p_0) = \sqrt{\frac{1}{2\pi} \int_{-\infty}^{\infty} |G_{cl}(i\omega)|^2 S_v(\omega) d\omega} \quad (42)$$

where  $S_v$  is the spectrum of the vertical heave velocity as given in (37).

Regarding the derivation of  $P$ , Laplace-transforming (1)–(6) in each well section  $j = 1, \dots, 4$  gives an ODE in  $z$  of the form

$$\frac{\partial}{\partial z} x_j(z, s) = \bar{A}_j(s) x_j(z, s) \quad (43)$$

where the states vectors are

$$x_j(z, s) = \begin{pmatrix} p_{a,j}(z, s) & q_{a,j}(z, s) & p_{i,j}(z, s) & q_{i,j}(z, s) \\ \sigma_{d,j}(z, s) & v_{d,j}(z, s) \end{pmatrix}^T, \quad j = 1, 2, 3 \quad (44)$$

$$x_4(z, s) = \begin{pmatrix} p_b(z, s) & q_b(z, s) \end{pmatrix}^T \quad (45)$$

The matrix  $\bar{A}_j(s)$  as well as others that are used in the following equations are given in Appendix B. Defining

$$z_{10} = z_{BHA}, z_{20} = z_{CV}, z_{30} = z_{CV}, z_{40} = z_{bit}, \quad (46)$$

the solution of (43) is of the form

$$x_j(z, s) = e^{\bar{A}_j(s)(z-z_{j0})} x_j(z_{j0}, s). \quad (47)$$

for  $z \in S_j$ . After linearizing (10)–(11) and (13), the topside boundary conditions can be written in the form

$$\begin{aligned} \bar{B}_{11}(s)x_1(L, s) &= \bar{B}_{11}(s)e^{\bar{A}_1(s)(L-z_{BHA})}x_1(z_{BHA}, s) \\ &= \bar{D}_1(s) \begin{pmatrix} v_{rig}(s) \\ q_{CV}(s) \end{pmatrix} \end{aligned} \quad (48)$$

and analogously for the coupling and boundary conditions at  $z_{BHA}$ ,  $z_{CV}$ ,  $z_{bit}$  and  $z = 0$ . Stacking all coupling and boundary conditions into one equation, the overall system can be written as

$$\Lambda(s)x^*(s) = D(s) \begin{pmatrix} v_{rig}(s) \\ q_{CV}(s) \end{pmatrix} \quad (49)$$

with

$$x^* = (x_1(z_{BHA}) \quad x_2(z_{CV}) \quad x_3(z_{CV}) \quad x_4(z_{bit}))^T. \quad (50)$$

After solving (49) for  $x^*$ , the outputs are obtained by use of (47), i.e.

$$p_0(s) = \Gamma_1(s)x^*(s), \quad \dot{v}_{CV}(s) = \Gamma_2(s)x^*(s). \quad (51)$$

If the objective is changed to controlling the pressure at a position different to the well bottom, the performance output can easily be changed to the pressure at an arbitrary position in the annulus or below the bit by modifying the  $\Gamma_1$  matrix. Finally, using  $\Gamma = (\Gamma_1 \quad \Gamma_2)^T$ ,

$$P(s) = \begin{pmatrix} p_{11}(s) & p_{12}(s) \\ p_{21}(s) & p_{22}(s) \end{pmatrix} = \Gamma(s)\Lambda^{-1}(s)D(s). \quad (52)$$

### 3. Controller design

Both dominant causes of downhole pressure oscillations – the dashpot-like movement of the BHA and mud sticking to the moving drillstring – are most appropriately described as flow disturbances rather than as accelerations. Therefore, we split the controller from BHA acceleration to controllable valve flow into two steps. First, a heave integrator, denoted by  $C_h$ , estimates the current BHA velocity from the measured acceleration. Second, a feedforward controller, denoted  $C_{vq}$  maps the estimated velocity to the desired controllable valve flow. The full controller from acceleration to flow is denoted by

$$C(s) = C_h(s)C_{vq}(s). \quad (53)$$

#### 3.1. Heave velocity estimation

Mathematically, the heave velocity can be obtained by simply integrating acceleration. In practice, this would result in drift of the mean of the estimated velocity due to measurement bias and noise. A better solution is given by a band-pass filter of the form

$$C_h = \frac{s}{s^2 + 2\zeta\omega_c s + \omega_c^2} \quad (54)$$

which acts like an integrator at high frequencies but ensures that there is no drift in the mean of the estimated velocity. Here, the cut-off frequency  $\omega_c$  is chosen slow enough such that the filter behaves like an integrator in the dominant frequency range of the heave motion. In this paper, we use  $\omega_c = 0.01$ , which is much slower than the heave frequency. Therefore, there is almost no error between real heave velocity and the velocity estimated from acceleration measurements. In practice, small error between actual and estimated heave velocity will be a requirement on the hardware used, although first lab-scale experiments (see also Figure 5 in Kvernland, Christensen, Borgen, Godhavn, Aamo, Sangesland, et al. (2018)) suggest that the heave velocity can be estimated relatively accurately in such a fashion and even better results should be expected with higher-quality hardware. Heave-estimator design tradeoffs taking into consideration the magnitude of noise and bias are also discussed in Godhaven (1998).

#### 3.2. Design of controller $v_{CV}$ to $q_{CV}$

##### 3.2.1. Nominal infinite-dimensional controller

Assume for now that the BHA velocity is directly available to the controller instead of estimated via the acceleration. This is a reasonable assumption because, as discussed above, we assume that the error between actual heave velocity and the velocity estimated by  $C_h$  using acceleration measurements is negligible.

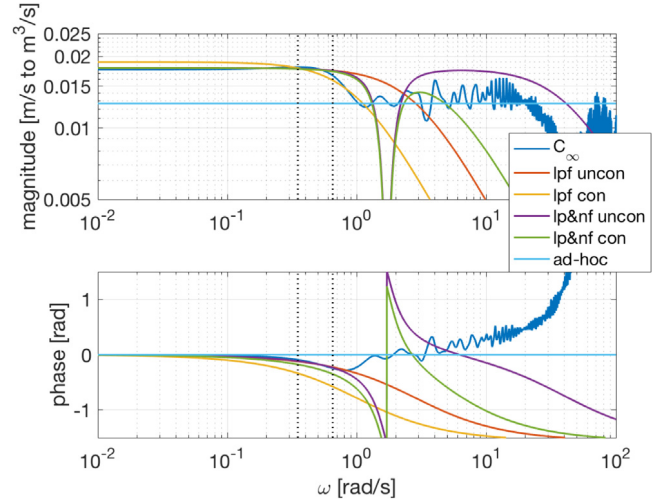


Fig. 5. Bode plot of  $C_\infty$  and the different low-order approximations (lpf=low-pass filter, lp&nf = low-pass and notch filters, uncon=unconstrained  $c_2$ , con = constrained  $c_2$ ). The black dotted lines indicate the frequency range of the heave disturbance.

The transfer functions from  $v_{rig}$  and  $q_{CV}$  to  $v_{CV}$  are  $\frac{1}{s}p_{21}(s)$  and  $\frac{1}{s}p_{22}(s)$ , respectively.

After closing the control loop, the pressure output  $p_0$  is given by

$$p_0(s) = \left( p_{11} + p_{12}C_{vq}(I - \frac{1}{s}p_{22}C_{vq})^{-1}\frac{1}{s}p_{21} \right) v_{rig}. \quad (55)$$

In an ideal case, the closed-loop transfer function from  $v_{rig}$  to output  $p_0$  should be zero. Mathematically, this can be achieved by setting the closed-loop transfer function from  $v_{rig}$  to  $p_0$  as given in (55) to zero and solving for  $C$ . This gives

$$C_\infty = s \frac{p_{11}}{p_{11}p_{22} - p_{12}p_{21}}. \quad (56)$$

However, the feedforward controller as given in (56) is infinite-dimensional and, hence, not implementable in practice. Therefore, a finite-order approximation of  $C_\infty$  is required.

##### 3.2.2. Low-order controller

In this paper we use a least-square approximation of  $C_\infty$  weighted by the disturbance spectrum. That is, we compute the finite-order controller by solving the optimization problem

$$\min_{C_{vq} \in \mathcal{C}} \int_0^\infty S_v(\omega) |C_{vq}(i\omega) - C_\infty(i\omega)|^2 d\omega \quad (57)$$

where  $\mathcal{C}$  is the set of permissible controllers of the desired structure. Since the computational power available downhole is limited, the dimension of the controller should be small. As can be seen in Fig. 3, the frequency range of the heave disturbance is relatively narrow. Therefore, good disturbance rejection can be achieved by a relatively low-order approximations of  $C_\infty$ . The velocity-to-flow controller  $C_{vq}$  obtained via (57) is then combined with the velocity estimator (54) to obtain the acceleration-to-flow controller  $C$  as in (53).

The Bode plots of  $C_\infty$  and  $\frac{1}{s}p_{22}$  are depicted in Figs. 5 and 6, respectively. At low frequencies,  $\frac{1}{s}p_{22}$  has almost constant gain and phase. Gain and phase then increase, starting approximately in the frequency range of the heave motion, with a first resonance at approximately  $\omega = 1.7$  rad/s. More resonances occur at higher frequencies, where the magnitude decreases very slowly with increasing frequency. The infinite-dimensional controller  $C_\infty$  is also approximately constant at low frequencies. Both gain and

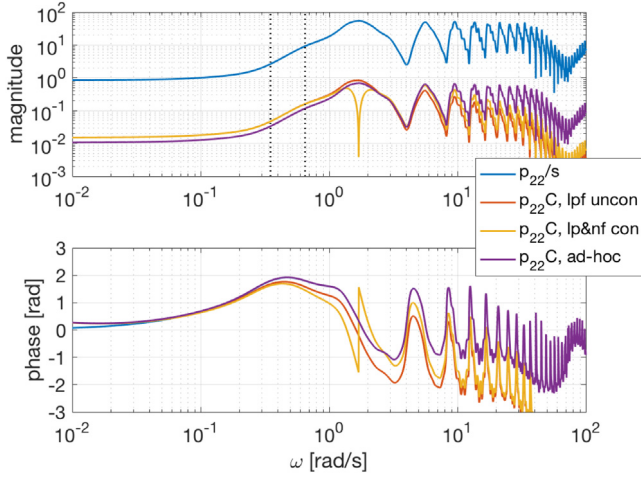


**Fig. 6.** Bode plot of  $p_{22}$  and of the feedback loop  $p_{22}C$  with  $C$  as in (53) using  $C_h$  as in (54) and different choices of  $C_{vq}$ .

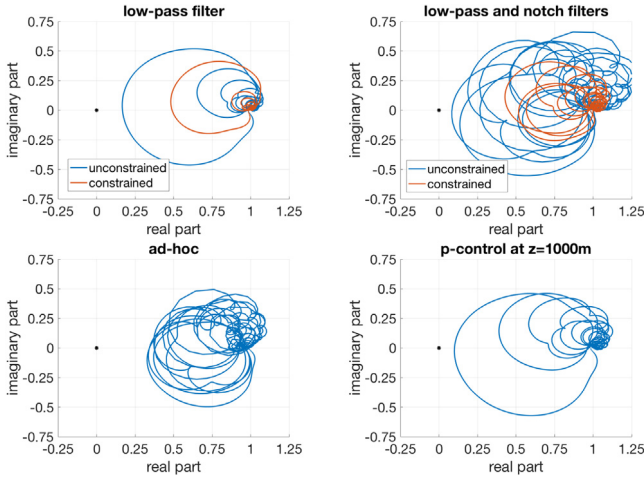


**Fig. 7.** Nyquist plot of the feedback loop  $1 - p_{22}C$  with  $C$  as in (53) using  $C_h$  as in (54) and different choices of  $C_{vq}$ .

**Table 4**

Comparison of the closed-loop performance for different controller choices.

$C_{vq} / C$	(58)	(59)	(60)	(61)	Ad-hoc	$C = 0$
rms( $p_0$ ) [bar]						
(frequency domain)	0.06	1.1	0.3	0.05	1.1	3.6
rms( $p_0$ ) [bar]						
(nonlinear simulation)	0.2	1.1	0.4	0.2	1.2	3.7

phase drop in the heave frequency range. In the following we discuss and compare different choices of controller form for  $C_{vq}$ : a low-pass filter and a low-pass filter combined with a notch filter. **Unconstrained low-pass filter.** Since  $C_\infty$  roughly resembles a low-pass filter at frequencies up to the heave disturbance, and in order to cancel resonances at higher frequencies, our first choice is to perform the optimization in (57) over the set of all low-pass filters, i.e.

$$C = \left\{ \frac{c_1}{c_2 s + 1} : c_1 \in \mathbb{R}, c_2 \geq 0 \right\}. \quad (58)$$

The Bode plot of the resulting first-order controller is also depicted in Fig. 5, and the Bode plot of the closed feedback loop  $Cp_{22}$  using this  $C_{vq}$  is shown in Fig. 6. Since this choice of  $C_{vq}$  matches the optimal  $C_\infty$  very closely, the closed loop-performance is very

good, with  $\text{rms}(p_0) \approx 0.06$  bar when computed via the transfer function and (42). In the simulation of the full nonlinear model, the root mean square of the bottomhole pressure deviation from steady state is slightly higher at 0.2 bar. See also Table 4. Stability of the closed-loop system can be tested via the Nyquist plot which is depicted in Fig. 7. By differentiating the total energy in the mud and elastic drillstring, it can be shown that the open-loop system with inputs  $v_{rig}$  and  $q_{CV}$  is stable. Thus, for stable controllers, the closed-loop system is stable if the Nyquist contour of  $1 - p_{22}C$  does not encircle the origin. The low-pass filter obtained by the optimization still has a relatively large gain at the frequency of the first resonance at  $\omega \approx 1.7$ , resulting in a peak gain of the feedback loop of approximately 0.83, and consequentially a rather small gain margin in case of modeling or actuator errors.

**Constrained low-pass filter.** The effect of the first resonance at  $\omega \approx 1.7$  rad/s can be reduced by limiting the roll-off frequency. For instance, a peak gain of  $p_{22}C$  of approximately 0.5 can be achieved by limiting the roll-off frequency to 1 rad/s, i.e. using

$$C = \left\{ \frac{c_1}{c_2 s + 1} : c_1 \in \mathbb{R}, c_2 = 1 \right\}. \quad (59)$$

However, this significantly affects the controller in the heave frequency range, resulting in a worse performance of  $\text{rms}(p_0) \approx 1.1$  bar.

**Constrained low-pass and notch filters.** A more subtle way of avoiding excitation of the first resonance is by use of a notch-filter. This can be realized by optimizing over the set

$$C = \left\{ \frac{c_1}{c_2 s + 1} \frac{s^2 + \omega_n^2}{s^2 + \zeta \omega_n s + \omega_n^2} : c_1 \in \mathbb{R}, c_2 \geq 0.2 \right\}. \quad (60)$$

where we use  $\omega_n = 1.7$  and  $\zeta = 0.5$  for the nominal parameter set. The parameter  $\zeta$  determines the width of the notch and is tuned to be wide enough to robustly cancel the resonance but narrow enough to avoid affecting the controller much in the frequency range of the heave motion. In order to limit the controller gain at the frequencies of higher resonances, we limit the roll-off frequency by the (active) constraint  $c_2 \geq 0.2$ . The notch filter and bound on the roll-off frequency affect performance slightly ( $\text{rms}(p_0) \approx 0.2$  bar), but robustness is improved considerably, see Figs. 6 and 7. Since the constraint on  $c_2$  is active in this example, the optimization is actually performed over the steady state gain  $c_1$  only.

**Unconstrained low-pass and notch filters.** If the roll-off frequency is left unconstrained, for comparison, i.e. using

$$C = \left\{ \frac{c_1}{c_2 s + 1} \frac{s^2 + \omega_n^2}{s^2 + \zeta \omega_n s + \omega_n^2} : c_1 \in \mathbb{R}, c_2 \geq 0 \right\}, \quad (61)$$

one obtains slightly better performance at the expense of higher gain at the frequencies of higher resonances, which again leads to relatively small gain margins (Fig. 5 through 7). In the remainder of the paper, we focus on the two designs using (58) and (60), that is the unconstrained low-pass filter and the constrained low-pass and notch combination, respectively.

**Ad-hoc controller.** For comparison, Figs. 5 through 7 and Table 4 also show performance and robustness for a simpler controller design and no control. An ad-hoc approach for designing the feed-forward controller  $C_{vq}$  would be to simply cancel the dashpot-like effect of the drillstring movement. Neglecting friction around the BHA, the drillstring movement displaces a volume equal to  $-(A_{d,1} + A_{i,1})v_{d,1}(x_{BHA}, t)$  at the bottom of the annulus. This flow disturbance can be canceled by use of

$$C_{vq}(A_{d,1} + A_{i,1}). \quad (62)$$

**Constant valve flow.** We will also compare performance to the case that the flow through the controllable valve is kept constant

at  $q_{mp}$ , which is equivalent to  $C = 0$ . By use of the ad-hoc controller design (62), the downhole pressure oscillations are reduced compared to the uncontrolled case ( $\text{rms}(p_0)$  from 3.6 bar to 1.1 bar), but not to the same level as the optimization-based designs.

#### 4. Controller performance analysis

##### 4.1. Performance in simulations of the nonlinear model

In the following, we further analyze the controller performance in simulations of the full nonlinear model. Fig. 8 shows the time series of the vertical heave velocity of the rig used in all simulations over a 5 min period. The bit follows the rig movement closely with a slightly larger amplitude due to resonances in the elastic drill string. The bit movement is almost identical for all controllers discussed above. The figure also shows the time series of the deviation of the bottomhole pressure from the mean value. In the uncontrolled case, the pressure oscillates with the heave motion by up to approximately  $\pm 8$  bar. Both the unconstrained low-pass filter (58) and the notch-filter combined with the constrained low-pass filter (60) suppress the oscillations of  $p_0$  to within  $\pm 1$  bar, with slightly better performance by the low-pass filter. The ad-hoc controller also achieves a significant reduction to within  $\pm 2.5$  bar. These results are in line with the trends in Table 4. Notably, in all simulations the pressure amplitude peaks exceed its root mean square significantly. The percentage of time when the time series of  $p_0$  exceeds  $\text{rms}(p_0)$  by a factor of  $\gamma$  or more is also depicted in Fig. 8. The downhole pressure exceeds  $\text{rms}(p_0)$  on average 35% of the time, exceeds  $1.5 \cdot \text{rms}(p_0)$  approximately 12% of the time and  $2 \cdot \text{rms}(p_0)$  less than 5% of the time. Such a statistic can be useful in practice when one might be interested in the amplitude of pressure peaks rather than only the rms value.

Also relevant in practice is the distribution of the pressure oscillations along the well rather than at only one location at the well bottom, and is given in Fig. 9. In the uncontrolled case, the pressure amplitude has a maximum at the bottom and decreases along the well. Both controllers (58) and (60) reject the pressure oscillations most effectively at the bottom, for which they are designed. Pressure amplitudes remain somewhat larger further up in the well, but still significantly smaller than in the uncontrolled case. By replacing the pressure output  $p_0$  in the transfer functions (see also Fig. 4) by the pressure at an arbitrary location in the annulus, for instance at  $z = 1000$  m, and following the same procedure in the controller design for the modified transfer functions, it is possible to design the controller that rejects the pressure oscillations at other locations than the well bottom. The result for such a design with an unconstrained low-pass filter is also shown in Fig. 9. The pressure amplitude at  $z = 1000$  m is reduced further at the expense of a slightly larger amplitude at  $z = 0$ . However, as shown in Fig. 7, robustness is worse than with the original design. That is, modifying the pressure output pushes the optimized controller parameters closer to the margin of stability. Introducing constraints on the controller parameter  $c_2$  as discussed above, all of which were active, leads to almost exactly the same controllers, and thus pressure amplitude profiles, as with  $p_0$  as performance output. That is, it is impossible to create the pressure profile of the black line in Fig. 9 with the same robustness margins as when using (60). This case can still be relevant in practice, though, if closed-loop instability is impossible due to mechanical friction in long horizontal wells.

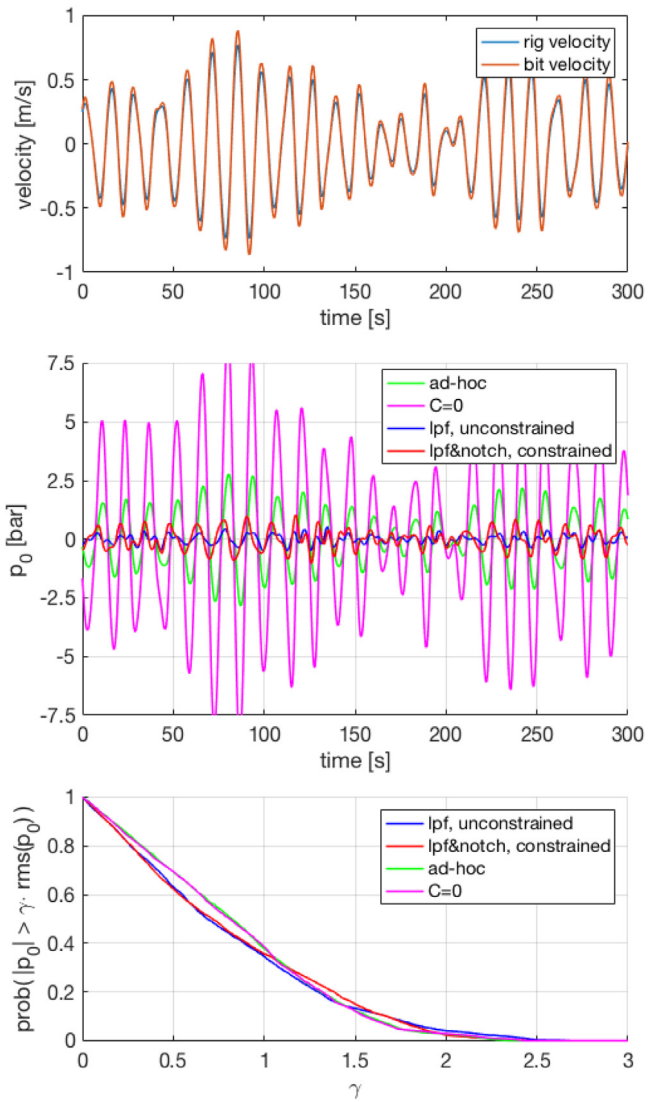


Fig. 8. Time series of rig and bit velocities, downhole pressures for different controller choices, as well as percentage of time when the downhole pressure time series exceeds  $\gamma \cdot \text{rms}(p_0)$ .

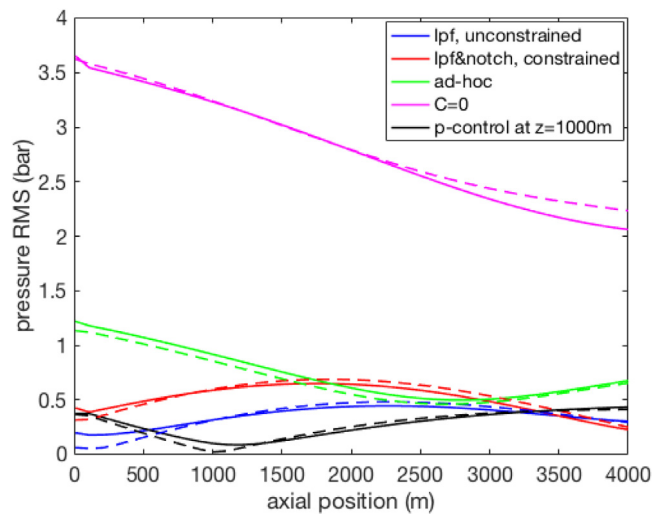


Fig. 9. Root mean square of the pressure plotted over the axial position. The solid lines are obtained from simulations of the nonlinear model while the dashed lines are according to the transfer functions and (42).

#### 4.2. Flow through controllable valve

Fig. 10 shows the time series of the flow through the controllable valve. The flow fluctuates considerably between approximately 500 l/min and 2500 l/min. The flows for the low-pass filter and low-pass and notch designs are very similar, while the ad-hoc controller induces smaller flow variations due to the smaller controller gain. There is usually a non-return valve installed in the bit in order to prevent particles such as rock cuttings from getting into the drillstring. Therefore, negative  $q_{CV}$  is impossible and the mean of  $q_{CV}$ , i.e. the main pump flow rate must be chosen large enough to ensure that  $q_{CV}$  stays away from zero. Fig. 10 also shows the coefficient of the controllable valve,  $c_{CV}$ , depending on the mean pressure drop over the valve, that is required to induce the flow for the low-pass and notch controller. Here, we assume that the flow is governed by a valve equation of the form

$$q_{CV} = c_{CV} \sqrt{\frac{\Delta p_{CV}}{\rho}} \quad (63)$$

where  $\Delta p_{CV}$  is the pressure drop over the controllable valve. The valve coefficient can be controlled via the opening of the valve. When increasing  $q_{CV}$ , a higher pressure drop over the bit causes a pressure build-up between bit and controllable valve, meaning that the valve must be opened further to provide the flow. If the mean of  $\Delta p_{CV}$  is chosen too low, such as 50 bar in this example, the required valve coefficient variations would become very large and even saturate during high waves. When increasing the mean of  $\Delta p_{CV}$  to 75 bar, the valve coefficient variations become feasible. Increasing  $\Delta p_{CV}^{mean}$  further decreases the variations of the valve opening. For instance, if the coefficient of a fully open valve is  $2 \times 10^{-3} \text{ m}^2$ , roughly 2.7 times the value of  $c_{bit}$  in this example, and assuming a linear valve characteristic, the valve opening would oscillate between approximately 5% and 65% for  $\Delta p_{CV}^{mean} = 75 \text{ bar}$  and approximately 5% and 35% for  $\Delta p_{CV}^{mean} = 100 \text{ bar}$ . Therefore, it is important to build up a sufficient pressure drop over the controllable valve prior to operation.

#### 4.3. Stability of closed-loop system

The purpose of this section is to further investigate stability of the closed-loop system in simulations, in particular the significance of nonlinearities in the model. Since fluid friction in the interior of the drillstring is quadratic in the flow rate, the transfer functions which are based on a linearization of the friction function tend to underestimate the stabilizing effect of friction. Moreover, mechanical friction in non-vertical wells can further stabilize the drillstring movement.

Fig. 11 shows the net fluid pressure forces acting on the BHA relative to the bit movement with and without control. Briefly speaking, pressure forces are in phase with the bit movement in case of control and in opposing phase without control. Without control, upwards movement of the BHA results in an increase in the fluid pressure above the BHA inside the string, and thus an increase in the pressure force acting downwards on the BHA and the controllable valve. Similarly, it causes a net decrease of the upwards pressure forces from below and from the annulus. That is, upwards movement of the BHA results in a net downwards force on the BHA, which dampens its movement. The controller, however, increases the flow through the controllable valve in case of upwards movement, mainly to compensate the displaced fluid. Therefore, the fluid pressure inside the drillstring decreases relative to steady case while the pressure forces from below and from the annular side are kept close to steady state. Thus, upwards bit movement leads to a net upwards force on the BHA. If this positive feedback mechanism is strong enough, in

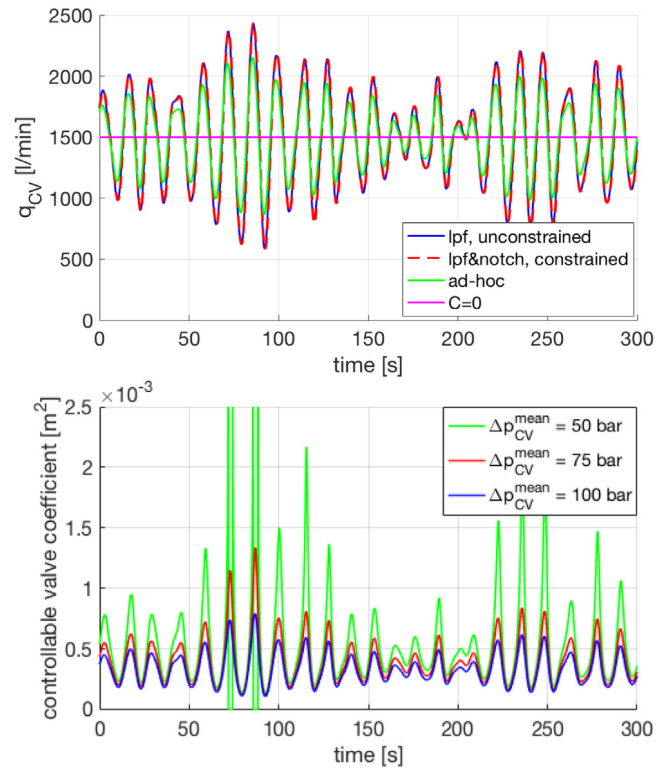


Fig. 10. Time series of  $q_{CV}$  and the discharge coefficient of the controllable valve for different differential pressures.

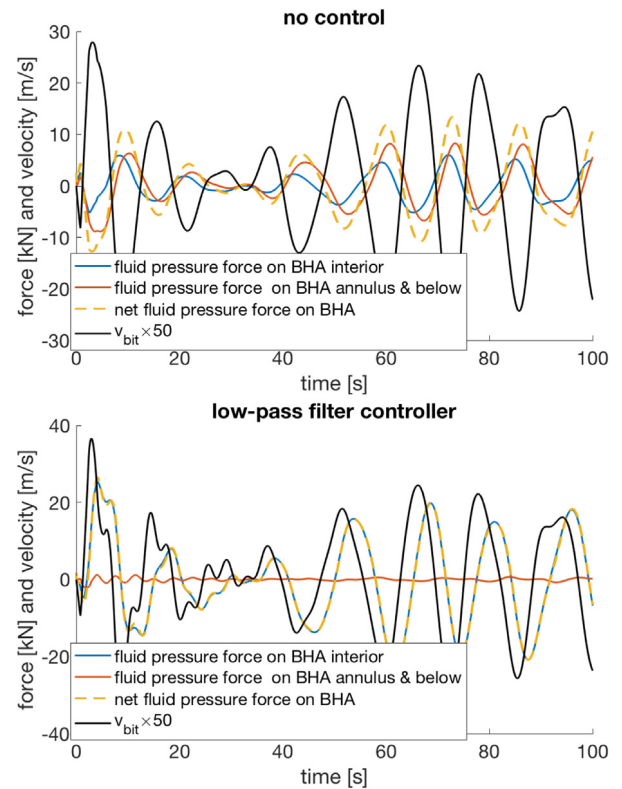


Fig. 11. Net upwards fluid pressure forces acting on the BHA assembly relative to upwards bit velocity.

particular when a resonant frequency is excited, it can destabilize the system.

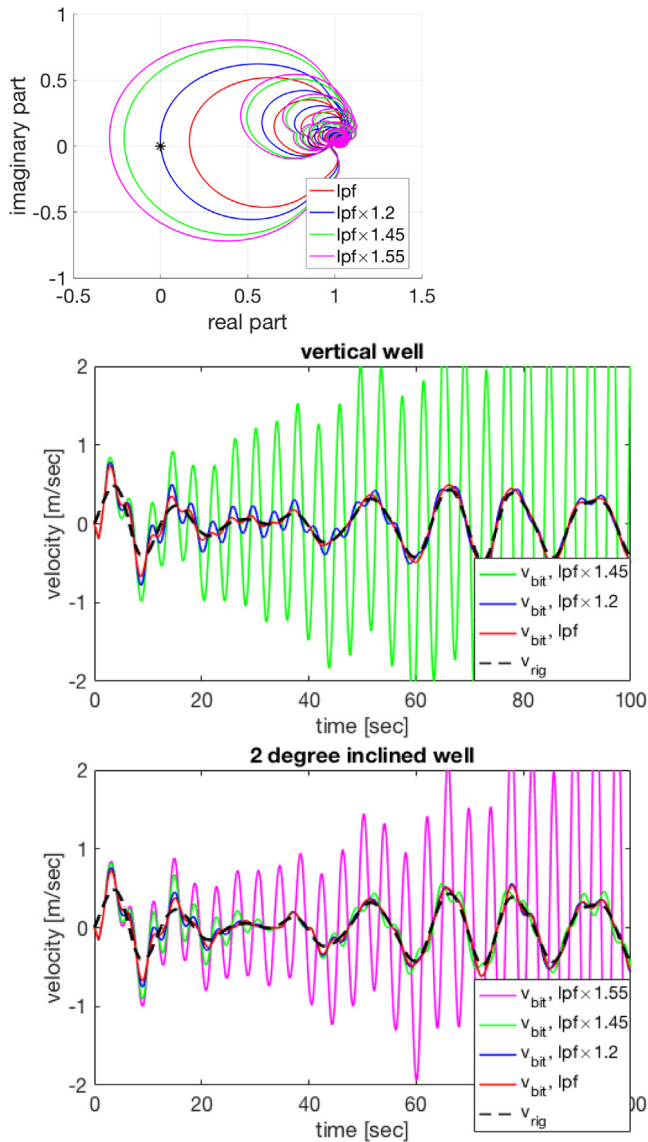


Fig. 12. Nyquist plot of the feedback loop using the low-pass filter multiplied by various factors, and the corresponding bit velocities obtained from simulations of the nonlinear model.

In the linear model, the closed-loop system becomes unstable if the Nyquist contour of  $1 - p_{22}C$  encircles the origin. In the following we test to which degree the Nyquist criterion agrees with stability observed in simulation of the nonlinear model, for the example with the unconstrained low-pass filter controller obtained via (58). As shown in Fig. 12, the Nyquist contour is at the margin of stability if the controller is multiplied by a factor of 1.2. In a vertical well, the trajectory of the bit velocity is still stable, but it exhibits some high-frequency oscillations around the trajectory when using the unmodified controller. If the multiplicative factor is increased, these oscillations become more severe, but remain stable. Divergence of the bit movement is observed from approximately a factor of 1.45 onwards, where the bit begins to oscillate with increasing amplitude in the frequency of the first resonance observed in the Bode plot of  $p_{22}$  at  $\omega = 1.7$  rad/s. While it is advisable to keep a reasonable margin from instability, it has to be considered in practice the vibrations observed at a factor of 1.2 can already be detrimental due to increased wear on the equipment.

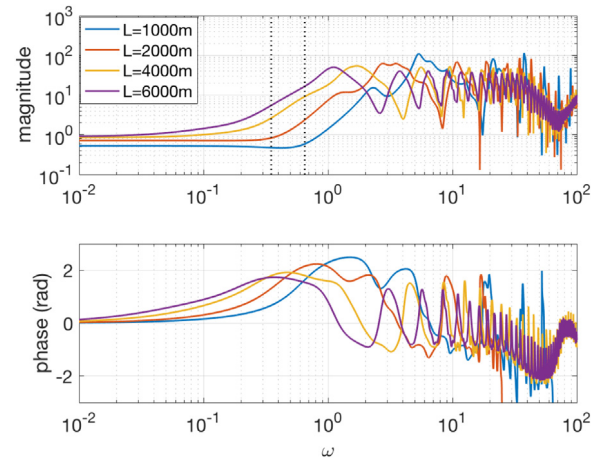


Fig. 13. Variation of  $\frac{1}{s}p_{22}$  with well length.

Since real wells are never perfectly vertical, there will always be mechanical drag dampening the drillstring movement. Fig. 12 also shows the trajectory of  $v_{bit}$  in a well that is inclined by 2 degree from vertical. Two degree inclination results in a 140 m horizontal displacement of the well bottom relative to the well head in the 4000 m deep well. In this well, the bit movement remains stable if the controller is multiplied by a factor of 1.45, but instability occurs from a factor of approximately 1.55 onwards. Thus, the stabilizing effect of mechanical friction is noticeable. However, the potentially destabilizing effect of the flow controller is still relevant in such near vertical wells.

#### 4.4. Variation with well length

During the drilling process, it is essential to be able to drill a whole section of up to several kilometers length. Therefore, it is important to understand how the system dynamics depend on well length. Moreover, controller performance can be improved by updating controller parameters as drilling progresses, instead of using one fixed controller for drilling a long section.

Fig. 13 shows how  $\frac{1}{s}p_{22}$  varies with the length of the well. The frequency of resonances, most importantly of the first resonance, increases the shorter well is. This can be directly related to the time pressure waves in the mud inside the drillstring take to propagate through the well. The magnitude of the transfer functions also varies slightly.

Nyquist plots of the closed loop system using the controller designs discussed above are shown in Fig. 14. When using the unconstrained low-pass filter design (58) or the ad-hoc controller (62), longer wells are more robustly stable, whereas a 2000 m deep well is right at the margin of stability when using these controllers, and render the closed-loop system unstable in a short 1000 m well. This dependence on well length can be attributed to a combination of the resonant frequency and the fact that the shorter the well, the less friction dampens pressure waves propagating through the well. Similar to the previous section, the Nyquist criterion roughly agrees with stability observed in simulations of the nonlinear model. By use of the constrained notch-filter design (60) with the same parameters  $\zeta = 0.5$  and  $c_2 \geq 0.2$  (the optimization constraint on  $c_2$  is active for all lengths tested here), stability is sufficiently robust in all cases. Here, the frequency of the notch-filter,  $\omega_n$ , is determined as the first resonance as depicted in Fig. 13. Due to better robustness, we focus on the design (60) in the following.

If communication between topside and the controllable valve is available, it is possible to update the controller as drilling

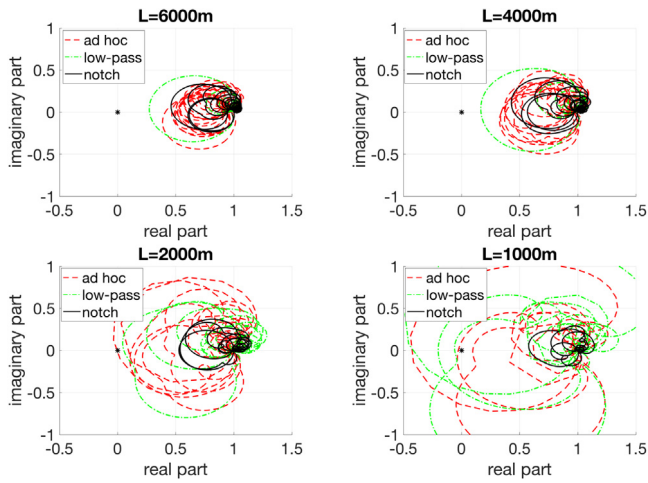


**Fig. 14.** Nyquist plots for different well lengths using the unconstrained low-pass filter (58), the constrained low-pass plus notch filter (60), and the ad-hoc controller (62).

**Table 5**

Dependence of performance on well length using the second-order parameterized controller coefficients, and using the ad-hoc controller and no control for comparison.

Well length [m]	1000	2000	3000	4000	5000	6000
rms( $p_0$ ) [bar]	0.5	0.45	0.4	0.4	0.5	0.4
rms( $p_0$ ), ad-hoc	Unstable	0.8	0.95	1.1	1.3	1.45
rms( $p_0$ ), $C = 0$	3.3	3.55	3.55	3.6	3.9	4.25

progresses. However, if no such communication is available, or breaks down, it is important to still be able to autonomously update the controller, where the well length can be determined for instance by detecting connections of new drillstring segments. The frequency of the notch-filter  $\omega_n$  as well as the controller coefficient  $c_1$  obtained from the optimization procedure is plotted over the well length in Fig. 15. As shown in the figure, it is possible to find an accurate second-order parameterization of these controller parameters over  $L$ . The Nyquist contours when using this parameterization are virtually the same as those in Fig. 14. Performance is given in Table 5. The magnitude of the remaining pressure oscillations varies slightly with well length, but not significantly.

**4.5. Sensitivity with respect to model uncertainty and actuation errors**

In this section we investigate the sensitivity of closed-loop performance and stability with respect to uncertainty in various parameters. In practice, many downhole parameters, such as friction and bulk modulus, are uncertain to a certain extent, or change over time. For instance, mud composition or the pressure drop over the annular choke might be changed intentionally during the drilling operation, but mud properties can also change unintentionally and unnoticed due to chemical reactions or temperature changes. Therefore, it is important that the controller performance is not excessively sensitive with respect to such uncertainties.

The sensitivity of the downhole pressure oscillations with respect to multiplicative uncertainty in the annular friction, friction inside the drillstring and in the mud bulk modulus is depicted in Fig. 16. Here, the nominal parameters are multiplied by a factor of  $1 + \Delta$ , and the controller is obtained by use of the constrained low-pass + notch filter controller design (60) and nominal parameters. In all three cases, the magnitude of the

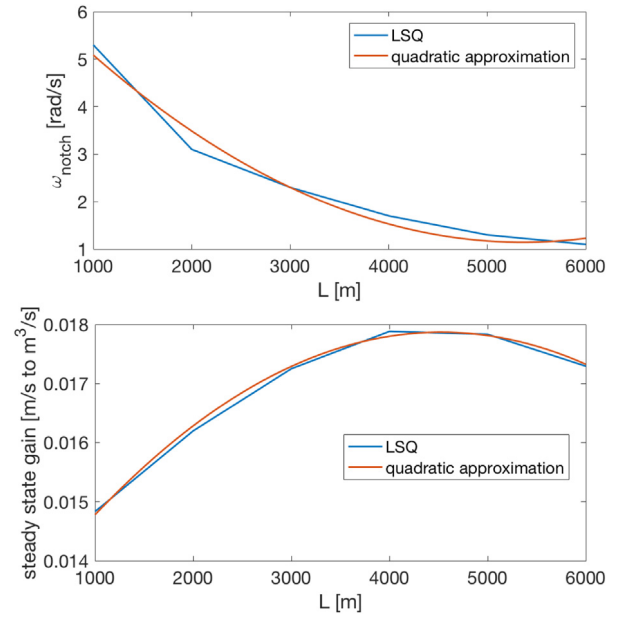


**Fig. 15.** Controller parameters depending on well length as obtained by least-squares optimization and second-order approximation.

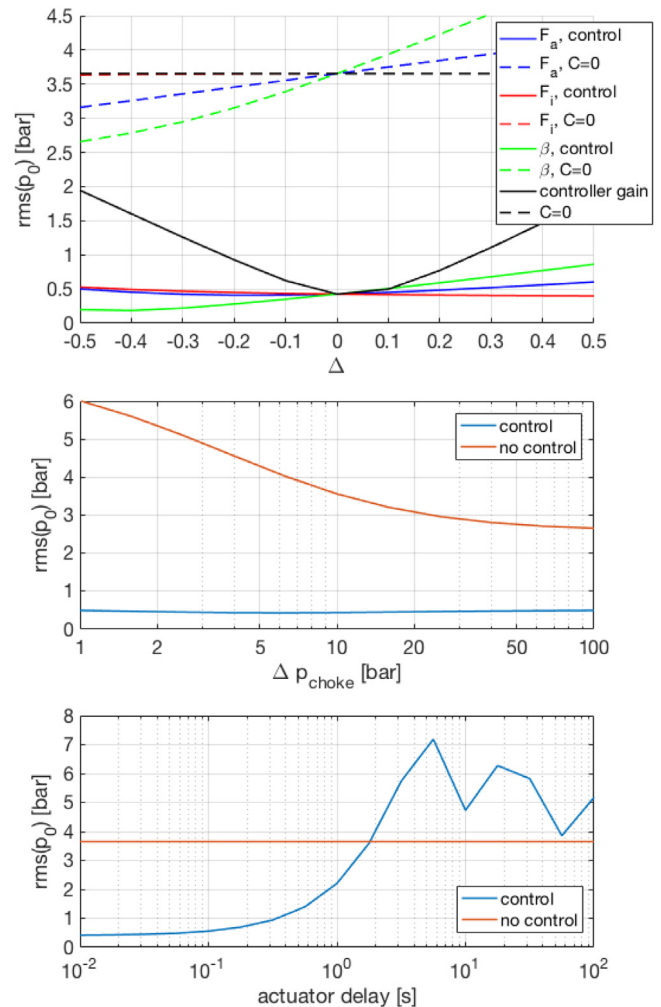


**Fig. 16.** Sensitivity of performance with respect to various parameters when using the constrained low-pass plus notch filter (60) tuned for nominal parameters, and without control.

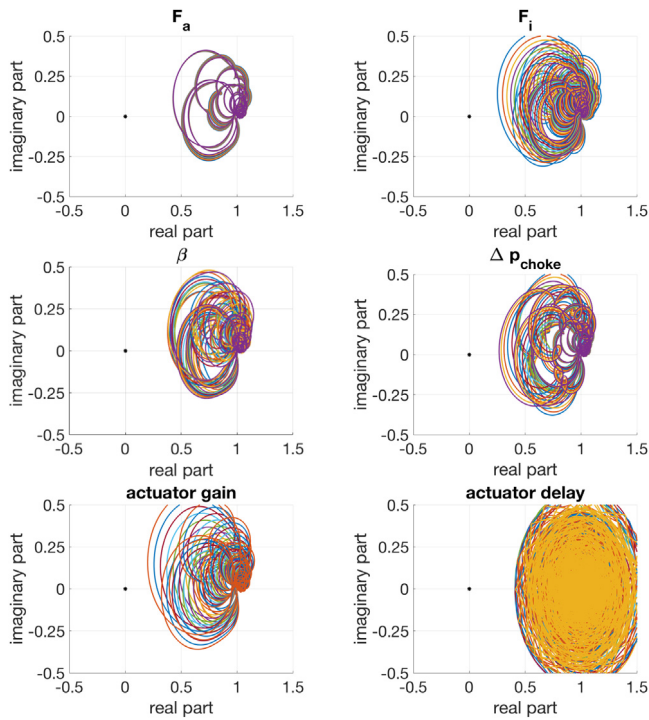


Fig. 17. Nyquist contour for all parameter samples from Fig. 16.

pressure oscillations is affected only little. For all three types of uncertainty, re-optimizing the controller for the actual, uncertain parameters brings only a marginal improvement compared to the controller that is designed for nominal parameters (not depicted in the figure). In the case of uncertainty of the bulk modulus, for instance, the sensitivity can be attributed to the fact that a larger bulk modulus generally results in larger pressure oscillations, as the same trend can also be seen in the case without control. The Figure also shows the sensitivity with respect to changes in the pressure drop over the annular choke,  $\Delta p_{choke}$ . This pressure drop is controlled via the choke opening, and is changed while drilling in order to adjust the mean value of the bottomhole pressure. Controller performance is also very insensitive with respect to such changes in this example. However, in other examples with very little friction in the annulus, performance can be more sensitive since the magnitude of potential pressure resonances depend on a combination of choke opening, well length and the annular friction parameters.

Sensitivity of the Nyquist contours is depicted in Fig. 17. Uncertainty in annular friction has almost no effect. Uncertainty in friction inside the drillstring, in contrast, has a more significant effect as it determines by how much pressure resonances inside the drillstring are dampened, which can apply a destabilizing force on the BHA. The effect of uncertainty in  $\beta$  and  $\Delta p_{choke}$  on robustness is moderate.

The previous analysis assumes exact actuation, where we have

$$q_{cv}(t) = q_{mp} + q_c(t) \quad (64)$$

where  $q_c(t)$  is the controller output at time  $t$ . Figs. 16 and 17 also show the sensitivity with respect to gain and delay errors in the heave-rejection controller, i.e.

$$q_{cv}(t) = q_{mp} + \delta \times q_c(t - \theta) \quad (65)$$

for gain error  $\delta$  and delay  $\theta$ . Due to the single-input single-output structure of the controller, the delay is the sum of delays in

sensing and actuation. Here, we assume that the mean of  $q_{cv}$  is held accurately at  $q_{mp}$ , for instance by a separate slower control loop keeping the interior pressure above the controllable valve constant. Both performance and robustness of stability are relatively sensitive to controller gain errors, significantly more sensitive than with respect to parametric errors considered above. Performance is similarly sensitive with respect to a delays of approximately 0.5 s or longer, while the effect of delays is hardly noticeable for delays of less than around 0.1 s. Since the controller gain is designed to be small, stability is robust with respect to delays.

#### 4.6. Inclined wells

Since mechanical friction between the drillstring, BHA and borehole wall is basically a step function in the drillstring velocity, it is not possible to find an accurate linear approximation. Therefore, mechanical friction is not considered in the transfer functions derived in Section 2.5, and thus in the controller design. However, many wells are non-vertical. In many situations, a well has a vertical section up to a certain depth and then a near-horizontal section through the reservoir. The well path of such a well is depicted in Fig. 18, along with the simulated bit movement and the downhole pressure oscillations. As the rig moves with the heaving motion, the tension in the drillstring first has to overcome drag in the more than 2000 m long horizontal section before the bit moves. The bit is at rest until enough tension builds up. Once the drag force is overcome, the built-up tension causes the bit to snap, resulting in a short velocity peak larger than the rig velocity and the bit velocity in the vertical case (compare to Fig. 8). This is also visible in the spectrum of the bit movement. Compared to the rig motion, the bit motion in case without control has a smaller peak at  $\omega = 0.5$ , but the bit velocity has additional components at a higher frequencies of around  $\omega = 1.4$ .

Fig. 18 also shows the downhole pressure trajectory both with and without control. Even though the controller design neglects mechanical friction, a significant improvement in the pressure oscillations is achieved. Due to the fact that the controller measures the BHA movement and thus, essentially, the disturbance, performance is relatively insensitive to errors in the drillstring model. This is a big difference to the case where the actuation is topside, which heavily relies on being able to predict the bit movement based on the model for drillstring elasticity. See Strecker and Aamo (2018) for comparison. The remaining pressure oscillations in Fig. 18 are slightly worse than in the nominal example in Fig. 8, though, since the controller gain is too small at the second frequency peak around  $\omega = 1.4$  rad/s, which is very close to the frequencies that are filtered out by the notch filter. In fact, it can be seen in Fig. 18 that with control, the downhole pressure oscillates with frequency  $\omega = 1.4$  rad/s while the lower frequency components are attenuated very well, whereas without control the pressure trajectory follows the bit movement more closely.

Due to the higher bit velocities, the control inputs are larger, both when using the low-pass filter and the low-pass with notch filter designs. The larger variations in  $q_{cv}$  cause larger forces on the BHA. Therefore, despite mechanical friction, the bit velocities when using control are slightly larger than without control. Yet, instabilities did not occur even when multiplying the controller gains with a factor of 2 (not depicted here). Thus, the low-pass filter design appears to be robustly stable in this case, and it is not necessary to introduce the notch filter at the expense of some performance.

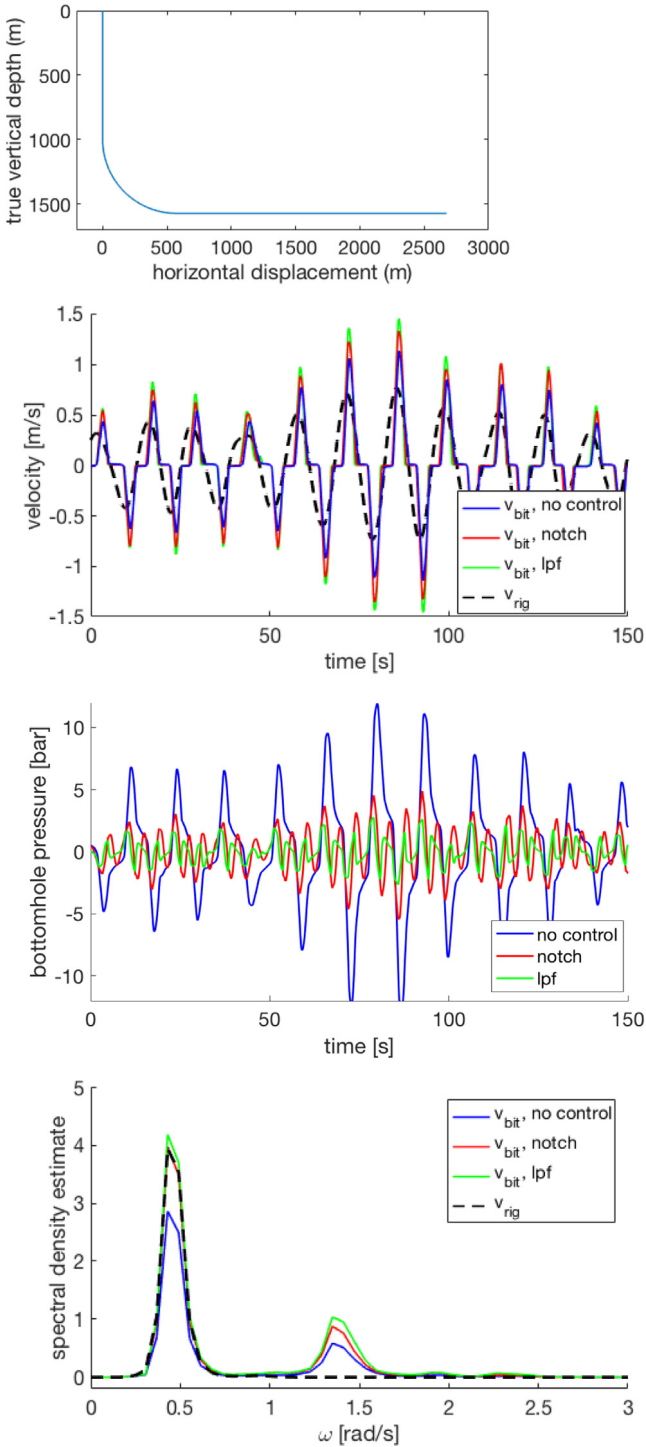


Fig. 18. Well path of a deviated well, simulated bit movement and pressure oscillations, and spectrum of the heave velocities.

### 5. Utilizing pressure feedback

The proposed controllable valve can not only measure acceleration but also mud pressures both on the inner and annular sides. In this section, we investigate to what extent feedback of the annular pressure next to the controllable valve can improve performance. Let  $p_{CV}$  denote the deviation of the annular pressure from steady state. In the previous examples, feedforward control, where the control input is computed based on the

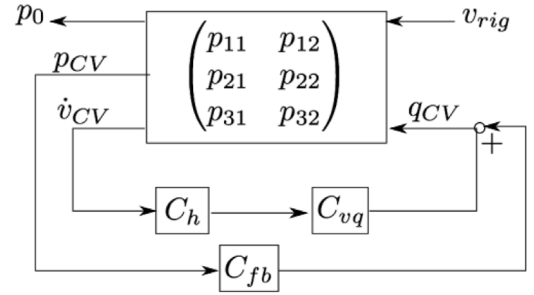


Fig. 19. Block diagram of the closed-loop system with both feedforward and feedback.

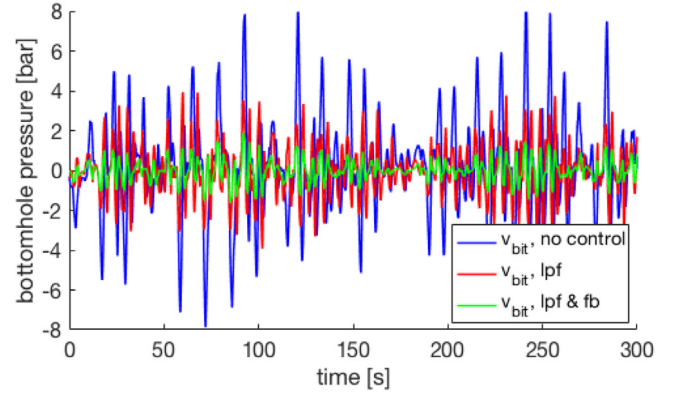


Fig. 20. Downhole pressure oscillations in deviated well like in Fig. 18 with and without pressure feedback.

measured bit movement rather than by feedback of the control error, achieves very good disturbance rejection. Performance is relatively sensitive with respect to actuation errors, but this is related to hardware limitations and hardly possible to improve by modifying the control architecture. One case where feeding the control error back into the control input can bring an advantage is in horizontal wells, where we have seen in Section 4.6 that the feedforward controller can fail to attenuate high-frequency components of the disturbance.

In order to design an example where the benefit of feedback is clearer, we change the choke coefficient and fluid rheology to  $C_{choke} = 3 \times 10^{-4} \text{ m}^2$ ,  $\tau_0 = 5 \text{ Pa}$  and  $K = 10 \text{ mPas}$ . This way, friction in the annulus is reduced and a pressure resonance in the annulus is created, similar to the high-frequency pressure oscillations observed in Fig. 18 but larger in magnitude. The corresponding pressure trajectories in open-loop and with the low-pass filter feedforward controller is shown in Fig. 20. The feedforward controller achieves a reduction in pressure oscillations from  $\text{rms}(p_0) \approx 2.4 \text{ bar}$  to  $\text{rms}(p_0) \approx 1.4 \text{ bar}$ , but is not as effective as in the previous case. The bit movement is almost the same as in Fig. 18.

It is straightforward to derive the extended transfer function  $P$  in Fig. 19 by following the same steps as in Section 2.5. We focus on the case where the bit is only a few meters above the well bottom, the controllable valve is installed close to the bit and friction around the BHA is small. Thus,  $p_{CV}$  is almost identical to  $p_0$ , and we can design the feedback controller to reject the oscillations of  $p_{CV}$ . The feedback controller should not control the mean of the downhole pressure, and have small gain at high frequencies to avoid sensitivity to noise and exciting high-frequency resonances. Therefore, we propose a band-pass filter of the form

$$C_{fb}(s) = -k \frac{s}{(s + \omega_1)(s + \omega_2)}. \quad (66)$$

The frequencies  $\omega_1 = 0.1$  rad/s and  $\omega_2 = 10$  rad/s are chosen to accommodate the heave spectrum and slightly higher frequencies. The minus sign in (66) is to reduce the flow  $q_{CV}$  if  $p_{CV}$  is too high and vice versa. Then, following a similar procedure as in Section 3.2, the gain  $k$  is designed so that the closed loop system is stable and has a similar gain margin as the unconstrained low-pass filter in Fig. 7, which gives  $k = 2 \times 10^{-7}$  m<sup>3</sup>/(sPa). Smaller  $k$  reduces effectiveness whereas larger  $k$  risks instability of the closed-loop system. The resulting downhole pressure oscillations in our example are shown in Fig. 20. The feedback controller achieves a reduction of rms( $p_0$ ) to approximately 0.5 bar, with almost no change in the bit movement.

## 6. Conclusion

In this paper, we considered the problem of attenuating heave-induced pressure oscillations by controlling the flow through a valve at the bottom of the drillstring based on the measured BHA motion. Changing the valve flow creates large differential pressures that can amplify the drillstring movement. A trade-off between performance and designing the control law to avoid exciting resonant, destabilizing frequencies is discussed. The proposed control law achieves a significant reduction in the pressure oscillations in the well. Due to the proximity of actuator and sensor to the well bottom, which is where the most pressure-sensitive part of the well is and where the piston-like effect of the drillstring movement occurs, performance is relatively insensitive to uncertainty in parameters and unmodeled mechanical friction in horizontal wells. If required, pressure feedback can be applied to improve attenuation of remaining pressure oscillations. When the cost for additional instrumentation is justified, the controllable valve can enable drilling operations in conditions where other methods, such as setting the choke opening to create a pressure antiresonance or pressure control from topside are insufficient.

## Acknowledgments

The authors would like to thank Martin Ø Christensen and Martin Kvernland from Heavelock AS, and Professor Sigbjørn Sangesland from the Department of Geoscience and Petroleum at NTNU for fruitful discussions.

## Appendix A. Coefficients for drillstring deformation

Variations in the fluid pressures cause ballooning and compression of the elastic string and the formation. Formulas for the changes in drill string internal and external diameter as well as length due to internal and external pressures are given in Young and Budynas (2002), Table 13.5, cases 1a and 1c. They can be used to derive the following expressions

$$\frac{\partial A_{a,j}}{\partial p_{a,j}} = \frac{2\pi r_{do,j}^2}{E} \left( \frac{r_{do,j}^2 + r_{di,j}^2}{r_{do,j}^2 - r_{di,j}^2} - \nu \right) + \frac{2\pi r_w^2}{E_f} (1 + \nu_f) \quad (67)$$

$$\frac{\partial A_{a,j}}{\partial p_{i,j}} = -\frac{4\pi r_{do,j}^2 r_{di,j}^2}{E(r_{do,j}^2 - r_{di,j}^2)} \quad (68)$$

$$\frac{\partial A_{i,j}}{\partial p_{a,j}} = -\frac{4\pi r_{do,j}^2 r_{di,j}^2}{E(r_{do,j}^2 - r_{di,j}^2)} \quad (69)$$

$$\frac{\partial A_{i,j}}{\partial p_{i,j}} = \frac{2\pi r_{di,j}^2}{E} \left( \frac{r_{do,j}^2 + r_{di,j}^2}{r_{do,j}^2 - r_{di,j}^2} + \nu \right) \quad (70)$$

$$\frac{\partial A_b}{\partial p_b} = \frac{2\pi r_w^2}{E_f} (1 + \nu_f) \quad (71)$$

$$\frac{\partial \varepsilon_{z,j}}{\partial p_{a,j}} = \frac{2\nu r_{do,j}^2}{E(r_{do,j}^2 - r_{di,j}^2)} \quad (72)$$

$$\frac{\partial \varepsilon_{z,j}}{\partial p_{i,j}} = \frac{2\nu r_{di,j}^2}{E(r_{do,j}^2 - r_{di,j}^2)} \quad (73)$$

For a given mud bulk modulus  $\beta$  under atmospheric conditions, the effective bulk modulus for mud inside string, mud in annulus and mud below bit are

$$\beta_{a,j} = \beta \left( 1 + \frac{\beta}{A_{a,j}} \frac{\partial A_{a,j}}{\partial p_{a,j}} \right)^{-1} \quad (74)$$

$$\beta_{i,j} = \beta \left( 1 + \frac{\beta}{A_{i,j}} \frac{\partial A_{i,j}}{\partial p_{i,j}} \right)^{-1} \quad (75)$$

$$\beta_b = \beta \left( 1 + \frac{\beta}{A_b} \frac{\partial A_b}{\partial p_b} \right)^{-1} \quad (76)$$

## Appendix B. Matrices for Laplace-transformed system

Define the friction factors as follows (see also Section 2.3 and Strecker et al. (2017) for more details on the friction terms)

$$f_{aa,j} = \frac{\partial F_{a,j}}{q_{a,j}} \quad f_{ad,j} = -\frac{\partial F_{a,j}}{v_{d,j}} \quad (77)$$

$$f_{ii,j} = \frac{\partial F_{i,j}}{q_{i,j}} \quad f_{id,j} = -\frac{\partial F_{i,j}}{v_{d,j}} \quad (78)$$

$$f_{da,j} = \frac{\partial F_{d,j}}{q_{a,j}} \quad f_{di,j} = -\frac{\partial F_{d,j}}{v_{i,j}} \quad (79)$$

$$f_{dd,j} = \frac{\partial F_{d,j}}{v_{d,j}} \quad f_b = -\frac{\partial F_b}{q_b} \quad (80)$$

where the derivatives are taken at flow rate =  $q_{pump}$  (except for the subsystem below the bit, where the nominal flow rate is zero) and string/BHA velocity = 0, and the signs are chosen such that all friction factors are positive (See Eqs. (81) and (82) given in Box 1).

$$\bar{A}_4(z, s) = \begin{pmatrix} 0 & -\frac{s\rho_b + f_{b,j}}{A_b} \\ -s\frac{A_b}{\beta_b} & 0 \end{pmatrix} \quad (83)$$

$$\bar{B}_{11}(s) = \begin{pmatrix} 0 & 0 & 0 & 0 & 0 & 1 \\ 0 & 0 & s\frac{c_{acc}}{p_{mp}} & p_{mp} & 0 & p_{mp}A_{i,1} \\ -k_c & 1 & 0 & 0 & 0 & 0 \end{pmatrix} \quad (84)$$

$$\bar{B}_{21}(s) = \begin{pmatrix} 0 & 1 & 0 & 0 & 0 & 0 \\ 0 & 0 & 0 & 1 & 0 & 0 \\ 1 & 0 & 0 & 0 & 0 & 0 \\ 0 & 0 & 1 & 0 & 0 & 0 \\ 0 & 0 & 0 & 0 & 0 & 1 \\ A_{a,1-2} & 0 & A_{i,1-2} & 0 & -A_{d,1} & 0 \end{pmatrix} \quad (85)$$

$$\bar{B}_{22}(s) = \begin{pmatrix} 0 & -1 & 0 & 0 & 0 & -A_{a,1-2} \\ 0 & 0 & 0 & -1 & 0 & -A_{i,1-2} \\ -1 & 0 & 0 & 0 & 0 & 0 \\ 0 & 0 & -1 & 0 & 0 & 0 \\ 0 & 0 & 0 & 0 & 0 & -1 \\ 0 & 0 & 0 & 0 & A_{d2} & 0 \end{pmatrix} \quad (86)$$

$$\bar{B}_{32}(s) = \begin{pmatrix} 0 & 0 & 0 & 1 & 0 & A_{i,2} \\ 0 & 0 & 0 & 0 & 0 & 0 \\ 0 & 1 & 0 & 0 & 0 & 0 \\ 0 & 0 & 0 & 0 & 0 & 1 \\ 1 & 0 & 0 & 0 & 0 & 0 \\ 0 & 0 & A_{i,2} & 0 & -A_{d,2} & 0 \end{pmatrix} \quad (87)$$

$$\bar{A}_j(z, s) = \begin{pmatrix} 0 & -\frac{s\rho_{a,j}+f_{aa,j}}{A_{a,j}} & 0 & 0 & 0 & \frac{f_{ad,j}}{A_{a,j}} \\ -s\frac{A_{a,j}}{\beta_{a,j}} & 0 & -s\frac{\partial A_{a,j}}{\partial p_{i,j}} & 0 & 0 & 0 \\ 0 & 0 & 0 & \frac{s\rho_{i,j}+f_{ii,j}}{A_{i,j}} & 0 & \frac{f_{id,j}}{A_{i,j}} \\ s\frac{\partial A_{i,j}}{\partial p_{a,j}} & 0 & s\frac{A_{i,j}}{\beta_{i,j}} & 0 & 0 & 0 \\ 0 & -\frac{f_{da,j}}{A_{d,j}} & 0 & \frac{f_{di,j}}{A_{d,j}} & 0 & s\rho_{d,j} + \frac{f_{dd,j}}{A_{d,j}} \\ -s\frac{\partial \varepsilon_{z,j}}{\partial p_{a,j}} & 0 & -s\frac{\partial \varepsilon_{z,j}}{\partial p_{i,j}} & 0 & \frac{s}{E} & 0 \end{pmatrix} \quad j = 1, 2, 3 \quad (81)$$

$$\Lambda(s) = \begin{pmatrix} \bar{B}_{11}(s)e^{\bar{A}_1(s)(L-z_{BHA})} & 0 & 0 & 0 \\ \bar{B}_{21}(s) & \bar{B}_{22}(s)e^{\bar{A}_2(s)(z_{BHA}-z_{CV})} & 0 & 0 \\ 0 & \bar{B}_{32}(s) & \bar{B}_{33}(s) & 0 \\ 0 & 0 & \bar{B}_{43}(s)e^{\bar{A}_3(s)(z_{bit}-z_{CV})} & \bar{B}_{44}(s) \\ 0 & 0 & 0 & \bar{B}_{54}(s)e^{-\bar{A}_4(s)z_{bit}} \end{pmatrix} \quad (82)$$

Box I.

$$\bar{B}_{33}(s) = \begin{pmatrix} 0 & 0 & 0 & 0 & 0 & 0 \\ 0 & 0 & 0 & 1 & 0 & A_{i,2} \\ 0 & -1 & 0 & 0 & 0 & -A_{a,2-3} \\ 0 & 0 & 0 & 0 & 0 & -1 \\ -1 & 0 & 0 & 0 & 0 & 0 \\ 0 & 0 & -A_{i,3} & 0 & A_{d,3} & 0 \end{pmatrix} \quad (88)$$

$$\bar{B}_{43}(s) = \begin{pmatrix} 0 & 0 & -k_b & 1 & 0 & A_{i,3} \\ 0 & 1 & -k_b & 0 & 0 & A_{d,3} + A_{i,3} \\ 1 & 0 & 0 & 0 & 0 & 0 \\ 0 & 0 & A_{i,3} & 0 & -A_{d,3} & 0 \end{pmatrix} \quad (89)$$

$$\bar{B}_{44}(s) = \begin{pmatrix} k_b & 0 \\ k_b & -1 \\ -1 & 0 \\ -(A_{d,3} + A_{i,3}) & 0 \end{pmatrix} \quad (90)$$

$$\bar{B}_{54}(s) = (0 \quad 1) \quad (91)$$

$$\bar{D}_1 = \begin{pmatrix} 1 & 0 \\ 0 & 0 \\ 0 & 0 \end{pmatrix} \quad \bar{D}_3 = \begin{pmatrix} 0 & 1 \\ 0 & 1 \\ 0 & 0 \\ 0 & 0 \\ 0 & 0 \\ 0 & 0 \end{pmatrix} \quad \bar{D} = \begin{pmatrix} \bar{D}_1 \\ 0_{6 \times 2} \\ \bar{D}_3 \\ 0_{5 \times 2} \end{pmatrix} \quad (92)$$

$$\Gamma_1(s) = (0_{1 \times 18} \quad (1 \ 0) \exp(-\bar{A}_4(s)z_{bit})) \quad (93)$$

$$\Gamma_2(s) = (0_{1 \times 11} \quad s \quad 0_{1 \times 8}) \quad (94)$$

References

Aadnoy, B., & Andersen, K. (1998). Friction analysis for long-reach wells. In *IADC/SPE drilling conference*. SPE-39391-MS.  
 Aamo, O. M. (2013). Disturbance rejection in  $2 \times 2$  linear hyperbolic systems. *IEEE Transactions on Automatic Control*, 58(5), 1095–1106.  
 Aarsnes, U. J. F., Aamo, O. M., Hauge, E., & Pavlov, A. (2013). Limits of controller performance in the heave disturbance attenuation problem. In *2013 european control conference* (pp. 1071–1076).  
 Aarsnes, U. J. F., Gleditsch, M. S., Aamo, O. M., & Pavlov, A. (2014). Modeling and avoidance of heave-induced resonances in offshore drilling. *SPE Drilling & Completion*, 29(04), 454–464.  
 Albert, A., Aamo, O. M., Godhavn, J.-M., & Pavlov, A. (2015). Suppressing pressure oscillations in offshore drilling: Control design and experimental results. *IEEE Transactions on Control Systems Technology*, 23(2), 813–819.  
 API Recommended Practice 13D (2006). *Rheology and hydraulics of oil-well drilling fluids*. Washington, DC: API.

Burkhardt, J. (1961). Wellbore pressure surges produced by pipe movement. *Journal of Petroleum Technology*, 13(06), 595–605.  
 Godhavn, J.-M. (1998). Adaptive tuning of heave filter in motion sensor. In *OCEANS'98 conference proceedings (Vol. 1)* (pp. 174–178). IEEE.  
 Godhavn, J.-M. (2010). Control requirements for automatic managed pressure drilling system. *SPE Drilling & Completion*, 25(03), 336–345.  
 Godhavn, J.-M., Pavlov, A., Kaasa, G.-O., & Rolland, N. L. (2011). Drilling seeking automatic control solutions. *IFAC Proceedings Volumes*, 44(1), 10842–10850.  
 Hannegan, D. M. (2006). CaSe studies-offshore managed pressure drilling. In *SPE annual technical conference and exhibition*. Society of Petroleum Engineers.  
 Hasselmann, K., Barnett, et al. (1973). *Measurements of wind-wave growth and swell decay during the Joint North Sea Wave Project (JONSWAP)*. Deutsches Hydrographisches Institut.  
 Herschel, W. H., & Bulkley, R. (1926). Konsistenzmessungen von gummi-benzollösungen. *Colloid & Polymer Science*, 39(4), 291–300.  
 Kvernland, M., Christensen, M., Borgen, H., Godhavn, J.-M., Aamo, O., Sangesland, S., et al. (2018). Attenuating heave-induced pressure oscillations using automated down-hole choking. In *IADC/SPE drilling conference and exhibition*. Society of Petroleum Engineers.  
 Kvernland, M., Gorski, D., Sant'Ana, M., Godhavn, J.-M., Aamo, O. M., Sangesland, S., et al. (2019). Verification of downhole choke technology in a simulator using data from a north sea well. In *SPE/IADC international drilling conference and exhibition*. Society of Petroleum Engineers.  
 Landet, I. S., Pavlov, A., & Aamo, O. M. (2013). Modeling and control of heave-induced pressure fluctuations in managed pressure drilling. *IEEE Transactions on Control Systems Technology*, 21(4), 1340–1351.  
 Mahdianfar, H., Hovakimyan, N., Pavlov, A., & Aamo, O. M. (2016).  $L_1$  adaptive output regulator design with application to managed pressure drilling. *Journal of Process Control*, 42, 1–13.  
 Mitchell, R. (1988). Dynamic surge/swab pressure predictions. *SPE Drilling Engineering*, 3(03), 325–333.  
 Pavlov, A., Kaasa, G.-O., & Imsland, L. (2010). Experimental disturbance rejection on a full-scale drilling rig. *IFAC Proceedings Volumes*, 43(14), 1338–1343.  
 Rehm, B., Schubert, J., Haghshenas, A., Paknejad, A. S., & Hughes, J. (2013). *Managed pressure drilling*. Elsevier.  
 Samuel, G. R., Sunthakar, A., McColpin, G., Bern, P., Flynn, T., et al. (2003). Field validation of transient swab-surge response with real-time downhole pressure data. *SPE Drilling & Completion*, 18(04), 280–283.  
 Starnes, O. N., Zhou, J., Kaasa, G.-O., & Aamo, O. M. (2008). Adaptive observer design for the bottomhole pressure of a managed pressure drilling system. In *Decision and control, 2008. CDC 2008. 47th IEEE conference on* (pp. 2961–2966). IEEE.  
 Stecki, J., & Davis, D. (1986a). Fluid transmission lines-distributed parameter models part 1: A review of the state of the art. *Proceedings of the Institution of Mechanical Engineers, Part A: Journal of Power and Energy*, 200(4), 215–228.  
 Stecki, J., & Davis, D. (1986b). Fluid transmission lines-distributed parameter models part 2: comparison of models. *Proceedings of the Institution of Mechanical Engineers, Part A: Journal of Power and Energy*, 200(4), 229–236.  
 Strecker, T., & Aamo, O. M. (2017a). Frequency domain analysis of backstepping-based disturbance rejection in a linear hyperbolic system. In *Australian & New Zealand control conference*.  
 Strecker, T., & Aamo, O. M. (2017b). Output feedback boundary control of  $2 \times 2$  semilinear hyperbolic systems. *Automatica*, 83, 290–302.

- Strecker, T., & Aamo, O. M. (2017c). Rejecting heave-induced pressure oscillations in a semilinear hyperbolic well model. In *American control conference, 2017* (pp. 1163–1168). IEEE.
- Strecker, T., & Aamo, O. M. (2018). Limitations of topside actuation for rejecting heave-induced pressure oscillations in offshore drilling. In *3rd IFAC workshop on automatic control in offshore oil and gas production*.
- Strecker, T., Aamo, O. M., & Manum, H. (2017). Simulation of heave-induced pressure oscillations in Herschel-Bulkley muds. *SPE Journal*, 22(05), 1–635.
- Wagner, R., Halal, A., Goodman, M., et al. (1993). Surge field tests highlight dynamic fluid response. In *SPE/IADC drilling conference*. Society of Petroleum Engineers.
- Young, W. C., & Budynas, R. G. (2002). *Roark's formulas for stress and strain* (Vol. 7). New York: McGraw-Hill.